





RESEARCH ARTICLE

The impact of aerosols and model grid spacing on a supercell storm from Swabian MOSES 2021

Christian Barthlott¹  | Beata Czajka¹ | Michael Kunz¹  | Harald Saathoff²  |
Hengheng Zhang² | Alexander Böhmländer² | Philipp Gasch¹ |
Jan Handwerker¹ | Martin Kohler¹ | Jannik Wilhelm¹  | Andreas Wieser¹ |
Corinna Hoose¹

¹Institute of Meteorology and Climate Research Tropospheric Research (IMKTRO), Karlsruhe Institute of Technology (KIT), Karlsruhe, Germany

²Institute of Meteorology and Climate Research Atmospheric Aerosol Research (IMKAAF), Karlsruhe Institute of Technology (KIT), Karlsruhe, Germany

Correspondence

Christian Barthlott, Institute of Meteorology and Climate Research Tropospheric Research (IMKTRO), Karlsruhe Institute of Technology (KIT), Karlsruhe, 76131, Germany.
Email: christian.barthlott@kit.edu

Funding information

Karlsruhe Institute of Technology

Abstract

The supercell storm that occurred in southwestern Germany on June 23, 2021, had an exceptionally long lifetime of 7.5 hr, travelled a distance of nearly 190 km, and produced large amounts of hail. During that summer, the Swabian MOSES field campaign was held in that area, and several hydro-meteorological measurements are available, as the storm passed directly over the main observation site. We present hindcasts of this event with the Icosahedral Non-hydrostatic model using two horizontal grid spacings (i.e., 2 km, 1 km) with a single-moment and an advanced double-moment microphysics scheme. Numerical results show that all 2 km model realizations do not simulate convective precipitation at the correct location and time. For the 1 km grid spacing, changes in aerosol concentration resulted in large changes in convective precipitation. Only the 1 km run assuming a low cloud condensation nuclei (CCNs) concentration is able to realistically capture the storm, whereas no supercell is simulated in the more polluted scenarios. Observed aerosol particle concentrations indicate that CCNs values were the lowest of the month, which suggests that the low aerosol concentration is a reasonable assumption. The thermodynamic structure of the pre-convective environment, as well as other observations, showed the best agreement to this model run as well, indicating that the good representation of the supercell was obtained for the right reason. The automatic tracking of individual clouds revealed that more convective cells with longer lifetimes are simulated at finer resolution. We also find a negative aerosol–precipitation effect that is not only due to a reduced collision–coalescence process, but also to weaker cold-rain processes. These findings demonstrate the benefits of using an aerosol-aware double-moment microphysics scheme for convective-scale predictability and that the use of different CCNs concentrations can determine whether a supercell is successfully simulated or not.

KEYWORDS

aerosol–cloud interactions, convection, cloud condensation nuclei, ICON model, supercell storm

This is an open access article under the terms of the [Creative Commons Attribution](https://creativecommons.org/licenses/by/4.0/) License, which permits use, distribution and reproduction in any medium, provided the original work is properly cited.

© 2024 The Authors. *Quarterly Journal of the Royal Meteorological Society* published by John Wiley & Sons Ltd on behalf of the Royal Meteorological Society.

1 | INTRODUCTION

Forecasting deep moist convection is still one of the key challenges in numerical weather prediction. In particular, the adequate forecast of supercell storms that often produce large hail, strong precipitation, and damaging winds is of great societal and economic relevance. A supercell is a specific type of intense, long-lived thunderstorm that is characterized by a persistently rotating updraught (e.g., Ashley et al., 2023). The predictability of convective precipitation is influenced by, for example, uncertainties in large-scale flow and approximations in the representation of key physical processes in numerical models. Several studies have noted the large impact of initial and lateral boundary conditions on the forecast of deep moist convection (e.g., Barthlott & Barrett, 2020; Bouttier & Raynaud, 2018; Richard et al., 2011). Large uncertainties also arise from the nonlinear character of the microphysics and aerosol–cloud interactions, which have been shown to vary with the environmental conditions, the aerosol regime, or cloud type (e.g., Altaratz et al., 2014; Barthlott & Hoose, 2018; Fan et al., 2016; Tao et al., 2012; van den Heever et al., 2011). Furthermore, boundary-layer processes are linked to aerosols also, as cloud condensation nuclei (CCNs) can influence the energy/radiation balance on the ground via effects on the number and size of cloud droplets, and thus on the cloud optical depth (e.g., Barthlott et al., 2022a; Kulmala et al., 2023). In addition, there are large uncertainties in the aerosol number concentration, as there are few in-situ observations or routine measurements of aerosols in three-dimensional space (Thompson et al., 2021). The role of aerosols in supercell thunderstorms is particularly important, as these storms can transport large amounts of moisture and heat through the atmosphere, and because of their potential to produce damaging winds, large hail, and weak-to-violent tornadoes. Recent studies have also shown that different assumptions for the amount of CCNs are relevant for quantitative precipitation forecasting and could be included in convective-scale ensemble prediction systems (Barthlott et al., 2022b; Baur et al., 2022; Keil et al., 2019; Matsunobu et al., 2022; Schneider et al., 2019).

During summer 2021, the Swabian Modular Observation Solutions for Earth Systems (MOSES) field campaign was conducted in southwestern Germany (Kunz et al., 2022). On June 23, 2021, a supercell initiated in the southern Black Forest and passed directly over several observational sites. The storm had an exceptionally long lifetime of 7.5 hr, travelled almost 190 km, and impacted large urban and rural areas with strong precipitation and hail. However, the predictability of this storm was rather low as the operational ensemble prediction system with 20 members (ICON-D2-EPS) of the Deutsche

Wetterdienst (German Weather Service, DWD) showed a large spread, thus giving only a small degree of confidence regarding the future weather development. Each member of ICON-D2-EPS is perturbed with respect to initial and boundary conditions, and model uncertainties are included by perturbing the model physics. The operational grid spacing for short-term numerical weather forecasts at the convective scale is currently 2 km, which is assumed to be sufficient to explicitly represent deep convection and no parametrization of deep convection is necessary (convection-permitting). However, it is unclear whether additional enhancements can be gained by decreasing grid spacings further to 1 km or below. Many studies indicate the potential benefits of higher model resolution to better simulate convective processes (e.g., Bennett et al., 2011; Done et al., 2004; Warren et al., 2014; Weisman et al., 2008). Decreasing horizontal grid spacing to 1 km has been shown to improve the representation of some features of convective systems; that is, more detailed and realistic reflectivities or updraughts (e.g., Barthlott et al., 2017; Barthlott & Davolio, 2016; Bryan et al., 2003; Bryan & Morrison, 2012; Schwartz et al., 2017). More recently, Weisman et al. (2023) compared forecasts of severe quasi-linear convective systems simulated using 1 km versus 3 km horizontal grid spacings to document the potential added value of such finer grid resolutions. They found that though many features of those convective systems can be reasonably represented at a grid scale of 3 km, some of the more detailed structures, such as overall reflectivity characteristics and the smaller leading-line mesoscale vortices, would likely benefit from the finer 1 km grid spacing.

Herein, we analyse numerical simulations of the well-observed supercell storm of June 23, 2021, from the Swabian MOSES field campaign with a focus on the precipitation sensitivity to grid spacing, as well as aspects of the bulk microphysics parametrization (single moment [1MOM] versus double moment [2MOM]). Hence, the goal of this article is to answer the following questions:

1. What is the influence of a higher grid resolution (horizontal and vertical) on convection initiation and subsequent precipitation? Are there general differences in convection-related parameters between the two grid spacings?
2. Does the forecast improve when a sophisticated 2MOM microphysics scheme is used instead of the operational 1MOM scheme?
3. What is the impact of aerosol–cloud interactions for quantitative precipitation forecasting, and is the inclusion of CCNs uncertainties relevant for ensemble prediction systems?

An important aspect of this work is the fact that the supercell passed directly over the main observation site

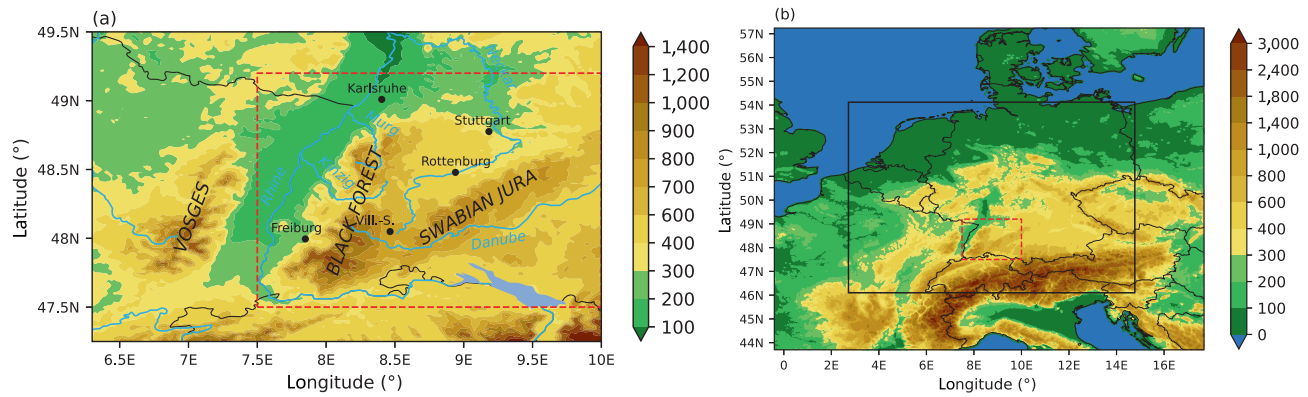


FIGURE 1 (a) Topography of southwestern Germany, eastern France, and northern Switzerland and (b) Icosahedral Non-hydrostatic model 2 km simulation domain with model topography in meters above sea level. The black rectangle in (b) depicts the 1 km simulation domain covering most of Germany and parts of neighbouring countries. The dashed rectangles indicate the domain of the Swabian MOSES 2021 field campaign. [Colour figure can be viewed at [wileyonlinelibrary.com](https://onlinelibrary.wiley.com)]

and that hail observations (size and number of hailstones), among others, are available for model evaluation. The remainder of this article is organized as follows: Section 2 describes the Swabian MOSES field campaign, the case of June 23, 2021, as well as the numerical model and experiments performed. The results are presented in Section 3. Section 4 contains a summary and conclusions.

2 | FIELD CAMPAIGN, CASE, AND SIMULATIONS OVERVIEW

2.1 | The Swabian MOSES field campaign

The field campaign Swabian MOSES was dedicated to hydro-meteorological measurements and was conducted by five Helmholtz research centres, three universities, and the DWD between May and September 2021 under the coordination of the Karlsruhe Institute of Technology (Kunz et al., 2022). The focus was on two hydro-meteorological extremes: (a) convective storms associated with heavy rainfall and hail, and (b) large-scale heat waves and associated droughts. MOSES is a novel observation system of the Helmholtz Association developed by the Helmholtz centres in the research field “Earth and Environment” (Weber et al., 2022). MOSES consists of highly flexible and mobile observation modules, such as the KITcube (Kalthoff et al., 2013), which are specifically designed to study the interactions of short-term events and long-term trends in different parts of the Earth system. The primary research goal of Swabian MOSES was to capture and explore the entire lifetime of events: from onset through its development to the stage of maturity and the associated impacts (such as consequences for agriculture and forestry or damage to infrastructure and property) to

the decay of the event. The investigation area was located in southwestern Germany (Figure 1). Previous studies of Kunz and Puskeiler (2010) and Puskeiler et al. (2016) have shown that severe hailstorms occur most frequently in the region south of Stuttgart and over the Swabian Jura, whereas hail activity is lowest over the Rhine valley and the low mountain ranges of the Black Forest. Based on a conceptual approach, the spatial differences in hail incidence were explained by a flow separation around the Black Forest for southwesterly directions at low Froude numbers. The associated downstream horizontal convergence at low levels and lifting of air then acts as convection initiation mechanism.

The observational systems deployed during Swabian MOSES comprised a variety of in-situ and remote-sensing systems, such as meteorological surface stations, towers, radiosoundings, wind and aerosol lidars, rain and cloud radars, disdrometers, and soil moisture sensors. Furthermore, two research aircraft were operated, one of them equipped with a scanning wind lidar. Eight in-situ hail sensors were deployed to measure hail size spectra with high temporal resolution. For a more detailed description of the Swabian MOSES instrumentation, the campaign strategy, and a summary of intensive observation periods, we refer to Kunz et al. (2022). Measurement campaigns dedicated to convective processes above complex terrain have already been carried out in this region; for example, VERTIKATOR (Meißner et al., 2007), PRINCE (Groenemeijer et al., 2009), or COPS (Richard et al., 2011; Wulfmeyer et al., 2011).

2.2 | Case and observations

In this study, we investigate the case of June 23, 2021, when a supercell was initiated over the southern Black Forest

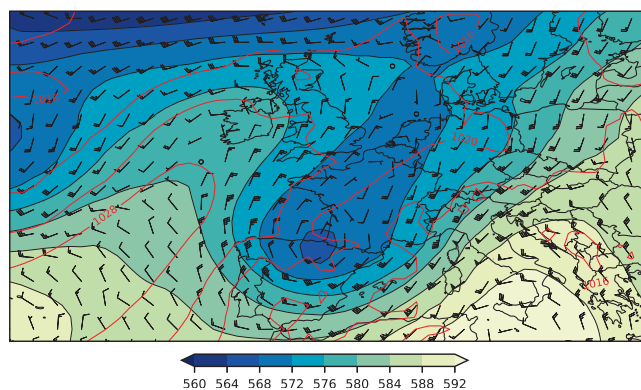


FIGURE 2 Global Forecast System analysis at 1200 UTC on June 23, 2021, showing 500 hPa geopotential height (gpm; shading), sea-level pressure (hPa; red contours), and 500 hPa wind barbs. [Colour figure can be viewed at [wileyonlinelibrary.com](https://onlinelibrary.wiley.com)]

and passed directly over several observational sites. This case was part of the Fourth Intense Observation Period lasting from June 17 to 24, 2021 (Kunz et al., 2022). On June 23, 2021, a slightly weakening trough stretched from southern Scandinavia towards southern Spain (Figure 2). During the day, a short-wave trough drifted along its eastern flanks and reached Germany around early afternoon. Together with mean-layer (i.e., averaged over the lowest 1 km) convective available potential energy (CAPE) increasing over the southwestern parts of the land around midday to about $950 \text{ J} \cdot \text{kg}^{-1}$, it facilitated the onset of deep convection. The wind in the middle troposphere over Germany was moderately strong and blew predominately from the southwest. At the surface, a vast high-pressure system over the North Atlantic stretched over western Europe towards northern Germany. A stationary front, a remnant of a multi-core low-pressure system from previous days that became associated with a surface low over Finland, lay across southern Germany (not shown) and remained there in the following days.

Figure 3a gives 24-hr accumulated precipitation from the RADOLAN (Radar Online Adjustment) precipitation analysis algorithm for June 23, 2021. This algorithm combines weather radar data with hourly surface precipitation observations from about 1,300 automatic rain gauges to obtain quality-controlled quantitative precipitation estimates. On this day, the first convective showers were initiated around 1300 UTC over the southern Black Forest, 13 km west of the city of Villingen-Schwenningen. In the first 2 hr, the showers travelled only slowly in a northeasterly direction. After 1450 UTC, the convective system gained speed and progressed further in an almost straight line towards the northeast. The cell started to decay around 2000 UTC and, at the same time, significantly reduced its displacement speed and turned to the east. Its life cycle

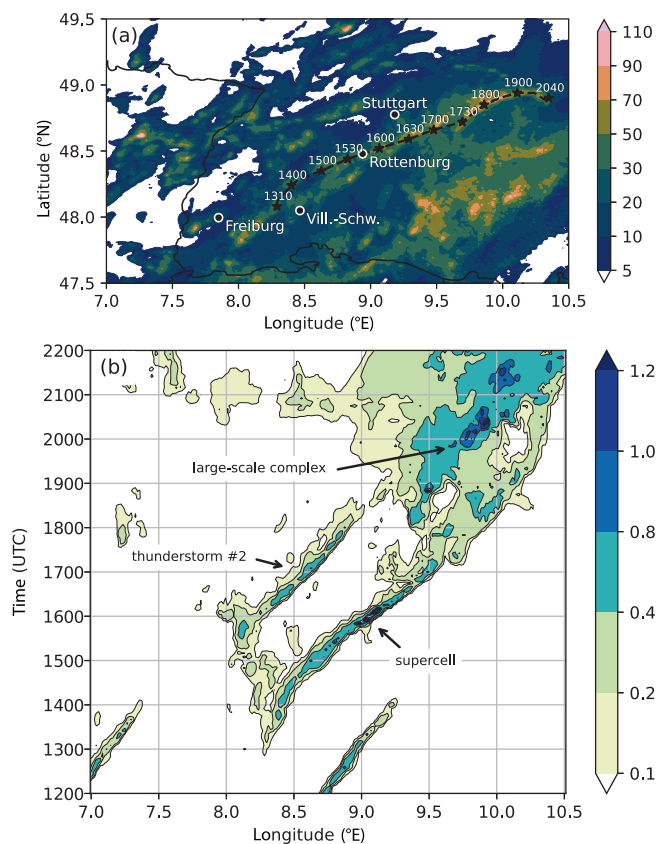


FIGURE 3 (a) RADOLAN (Radar Online Adjustment) observations of 24-hr accumulated precipitation with cell track (in mm) and (b) Hovmoeller diagram of mean precipitation averaged between 48 and 49.2° N (in mm/5 min). Vill.-Schw. in (a) denotes the city of Villingen-Schwenningen, and labelling of black stars indicate times (UTC). [Colour figure can be viewed at [wileyonlinelibrary.com](https://onlinelibrary.wiley.com)]

came to an end at 2045 UTC, which gives a total lifetime of 7.5 hr and a travel distance of 187 km. There were also convective showers with shorter lifetimes over the Vosges Mountains, the Rhine Valley, and the northern Black Forest. A second convective cell was initiated in the same region as the main supercell storm and moved slightly south of it in a northeasterly direction as well. This cell, however, had a shorter lifetime and decayed at around 1900 UTC. Furthermore, in the evening, convective cells moved into the MOSES domain from the south, merging into a large-scale convective system in the southeastern part of the MOSES domain. The temporal evolution of convective precipitation is given by the Hovmoeller diagram in Figure 3b.

Figure 4 shows the sounding launched from the Rottenburg site on July 23 at 1230 UTC. Clearly discernible is a dry middle and upper troposphere and a moderately moist lower troposphere. As a result of daytime heating, the air in the very lowest parts of the planetary boundary

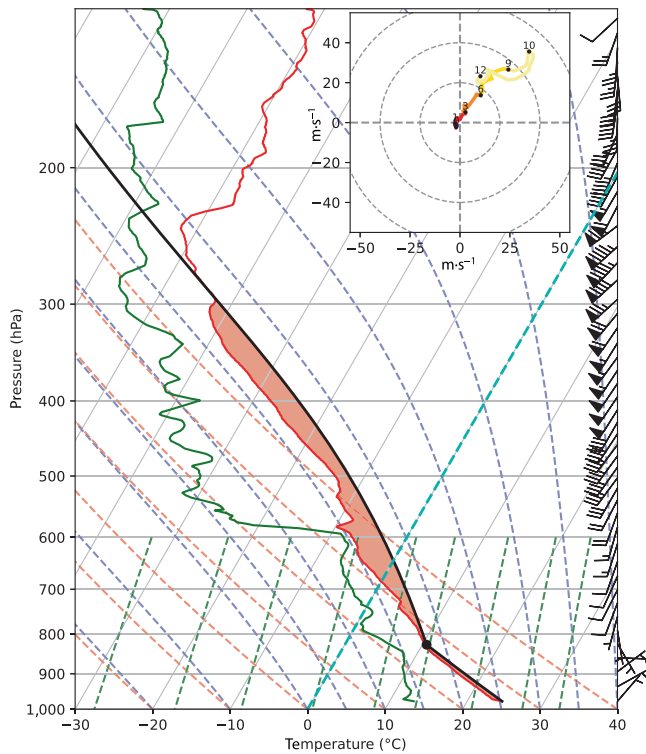


FIGURE 4 Skew- T -log P diagram and hodograph (inset) showing radiosonde profiles of temperature (red) and dew-point temperature (green), wind direction and speed (knots) at 1230 UTC June 23, 2021, at Rottenburg. The hodograph is colored by height intervals (purple: 0–1 km; red: 1–3 km; orange: 3–6 km; gold: 6–9 km; light yellow: 9–12 km). Image created using MetPy (May et al., 2022). [Colour figure can be viewed at wileyonlinelibrary.com]

layer (PBL) was already absolutely unstable at that time with a well-mixed boundary layer above. A pronounced directional wind shear was present in the lowest 250 hPa, as well as a strong vertical speed shear in the middle and upper troposphere. In general, the atmosphere over this part of Germany provided conditions favourable to the development of deep moist convection (with mean-layer convective inhibition $CIN = 11 \text{ J}\cdot\text{kg}^{-1}$, mean-layer CAPE = $469 \text{ J}\cdot\text{kg}^{-1}$). These values represent the mean potential energy conditions available to parcels of air located in the lowest 50 hPa when lifted to the level of free convection (LFC). The conditions for supercell development were also met, as the bulk Richardson number (BRN), which combines vertical wind shear through the lowest 6 km and CAPE, resulted in a value of 22. BRN values between 10 and 50 are considered to be conducive to supercell development (Weisman & Klemp, 1982). The 1116 UTC sounding from the nearby Stuttgart site (approximately 45 km northeast) also confirmed the possibility of supercell development, with BRN of 15, high surface-based CAPE ($886 \text{ J}\cdot\text{kg}^{-1}$), and no CIN, as well as moderate mean-layer CAPE ($291 \text{ J}\cdot\text{kg}^{-1}$) and low mean-layer CIN ($11 \text{ J}\cdot\text{kg}^{-1}$).

2.3 | Model description and simulations overview

All simulations of this study were performed with version 2.6.3 of the Icosahedral Non-hydrostatic (ICON) model (Zängl et al., 2015). ICON is based on an unstructured triangular grid and can be run in both global and limited-area mode with the possibility of online grid-nesting. We use two configurations at different horizontal and vertical resolutions that are both convection permitting: (a) 2 km R19B07 grid corresponding to the operational ICON-D2 configuration at the DWD, and (b) 1 km R19B08 grid nested into the former (Figure 1). The height-based terrain-following vertical coordinates are based on the vertically stretched smooth level vertical coordinate implementation (Leuenberger et al., 2010). The number of vertical levels is 65 at 2 km and 100 at 1 km horizontal grid spacing. The lowest model level in both configurations is located at 10 m above the ground, and 14 (18) levels lie in the first 1,000 m above ground for 65 (100) vertical levels. At 2 km grid spacing, deep convection is considered to be represented explicitly, but shallow convection is parametrized with the Tiedtke–Bechtold shallow convection scheme (Bechtold et al., 2008; Tiedtke, 1989). No convection schemes are used at 1 km grid spacing. We use a time step of 20 s at 2 km and 10 s at 1 km horizontal grid spacing. At the DWD, a 1MOM microphysics scheme is used for operational weather forecasting. This scheme includes riming processes and predicts cloud water, rain water, cloud ice, snow, and graupel. CCN activation is not simulated explicitly, and the condensed mass is determined by saturation adjustment (e.g., see Barthlott et al., 2017). We also use this scheme as a reference but conduct further simulations with the 2MOM microphysics scheme of Seifert and Beheng (2006) for the simulation of aerosol effects on liquid and mixed-phase clouds. This scheme predicts the number and mass concentrations of six different hydrometeor classes (cloud water, rain water, ice, snow, graupel, hail) and allows four different CCN concentrations for the investigation of aerosol–cloud interactions. As documented in Doms et al. (2021) and Seifert and Beheng (2006), 1MOM and 2MOM schemes use different parametrizations for microphysical conversion rates. For example, the autoconversion/accretion scheme in the 1MOM scheme assumes a constant cloud droplet number concentration of $200 \times 10^6 \text{ m}^{-3}$. Numerical simulations were conducted with four different number densities of CCNs, N_{CN} , representing low ($N_{CN} = 100 \text{ cm}^{-3}$), intermediate ($N_{CN} = 500 \text{ cm}^{-3}$), high ($N_{CN} = 1,700 \text{ cm}^{-3}$), and very high CCN concentrations ($N_{CN} = 3,200 \text{ cm}^{-3}$); for example, see Noppel et al. (2010). These concentrations are fixed in space and time, and only the indirect effects of aerosols are considered (i.e., aerosols do not directly

TABLE 1 Model configuration for the Icosahedral Non-hydrostatic (ICON) simulations.

Model aspect	Setting
Initial and boundary data	6.5 km ICON-EU analyses, 3 hr update
Initialization time	0000 UTC
Integration time	24 hr
Cloud condensation nuclei activation from aerosol particles	Using pre-calculated activation ratios stored in look-up tables (Segal & Khain, 2006)
Heterogeneous ice nucleation	Based on mineral dust concentrations (Hande et al., 2015)
Homogeneous ice nucleation	Following Kärcher and Lohmann (2002) and Kärcher et al. (2006)
Land-surface model	Multilayer land-surface scheme TERRA (Heise et al., 2006)
Turbulence parametrization	One-dimensional based on prognostic equation for the turbulent kinetic energy (Raschendorfer, 2001)
Radiation scheme	ecRAD (Hogan & Bozzo, 2018), called every 12 min

TABLE 2 Overview of the numerical simulations.

No.	Δx (km)	Microphysics	CCNs
1	2	1MOM	—
2	2	2MOM	Low
3	2	2MOM	Intermediate
4	2	2MOM	High
5	2	2MOM	Very high
6	1	1MOM	—
7	1	2MOM	Low
8	1	2MOM	Intermediate
9	1	2MOM	High
10	1	2MOM	Very high

Note: 1MOM and 2MOM denote single- and double-moment microphysics respectively; CCNs, cloud condensation nuclei.

affect radiation). The investigation of a heterogeneous distribution of aerosol across the domain, as applied by Schneider et al. (2019), is beyond the scope of the present study. We summarize further model settings in Table 1 and give an overview of all model runs in Table 2. In the following, the model runs are abbreviated according to three categories:

- grid spacing—2 km, 1 km;
- microphysics scheme—1MOM, 2MOM;
- CCNs concentration—low (low), intermediate (int), high (high), very high (vhig).

For example, the model run at 1 km grid spacing using the 2MOM scheme with low CCN concentration would then be referred to as 1km_2MOM_low.

3 | RESULTS

3.1 | Convective precipitation and supercell characteristics

At first, we assess the forecast quality of all 10 model runs with Hovmoeller diagrams (Figure 5).

It can be seen that all model runs operating at 2 km grid spacing fail to simulate the supercell. The model run using the operational 1MOM scheme produces precipitation too early in the longitude region where convection initiation occurs (Figure 5a). The convective activity ceases before 1400 UTC. The second thunderstorm, however, is relatively well captured by the model, but with a shorter lifetime. The simulated large-scale convective clusters moving in from the southern part of the MOSES domain in the evening are too weak and with a smaller horizontal extent

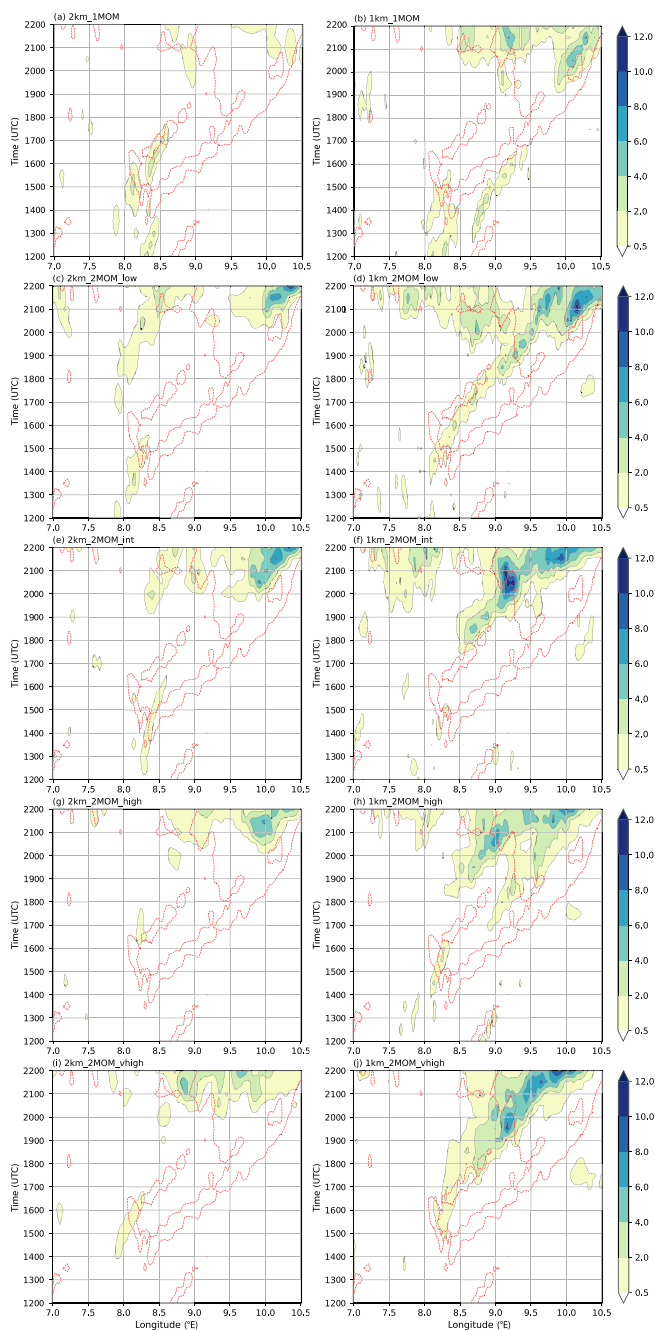


FIGURE 5 Hovmoeller diagrams of simulated precipitation amounts in mm/30 min for (a, c, e, g, i) 2 km and (b, d, f, h, j) 1 km grid spacing. Red dashed contours indicate the radar-derived mean precipitation of 1 mm/30 min. [Colour figure can be viewed at wileyonlinelibrary.com]

than observed. The simulation of this evening convection is improved by using the 2MOM scheme (Figure 5c,e,g,i), but these runs also fail to reproduce the supercell storm of interest. Going to a finer resolution of 1 km with a 1MOM scheme improves the simulation slightly (Figure 5b): there is a convective cell that is initiated 0.5° towards the east of the observed location. However, this cell is simulated too early and it dissolves too quickly at 1700 UTC. A much

better result is achieved when using the 2MOM scheme at 1 km grid spacing and assuming a low CCNs concentration (Figure 5d). In this model run, the time of convection initiation agrees well with observations and there is only a small horizontal displacement to the west (approximately 0.25°). The cell propagation towards the northeast is slowed down in the first 2 hr of its existence, leading to temporal delay of the supercell. At about 2200 UTC, the supercell merges with convective cells from the south. As will be shown later, the location in both longitude and latitude matches the observations rather well. The 1 km model run assuming an intermediate CCNs concentration (Figure 5f) produces some rain at a similar location and time as the run with low CCNs concentration. With this configuration, however, the convective clouds dissipate quickly and no supercell storm is simulated. Only after 1730 UTC is there a large convective cluster moving into the MOSES domain from France near the Swiss border. The model run assuming a high CCNs concentration (Figure 5h) shows a precipitating cloud system that lasted 2 hr in the area of convection initiation. But as in the aforementioned run, no long-lasting supercell storm is simulated and convective cells move into the MOSES domain later in the evening from France and from Switzerland. At first glance, the run with very high CCNs concentration also gives a reasonable result (Figure 5j). However, precipitation starts later than observed and also more in the north between the northern and southern Black Forest; that is, over the Kinzig Valley (see Figure 1). At the same time, a large convective cloud cluster comes in from France. Both travel towards northeast and merge at around 2000 UTC south of the city of Stuttgart. Again, convective showers move from Switzerland into the MOSES domain in the evening. Moreover, assuming a very high CCNs concentration results in too little precipitation in the Rhine Valley (not shown).

To clarify the impact of the higher vertical resolution and the shallow convection scheme on the simulation results, we performed additional model runs with a grid spacing of 2 km, 100 vertical levels, no shallow convection parametrization, and using all four different CCNs concentrations. These runs did not contain any supercell signatures or other visible model improvements (not shown). We therefore conclude that the improved result at a grid spacing of 1 km is not due to any one of these aspects, but the increase in resolution (i.e., horizontal and vertical and turning off the shallow convection parametrization) along with the more sophisticated 2MOM microphysics scheme are important to produce an adequate model representation of the supercell observed that day.

For a quantitative forecast verification, we computed the fractions skill score (FSS; Roberts & Lean, 2008; Matsunobu et al., 2022) comparing the model output with

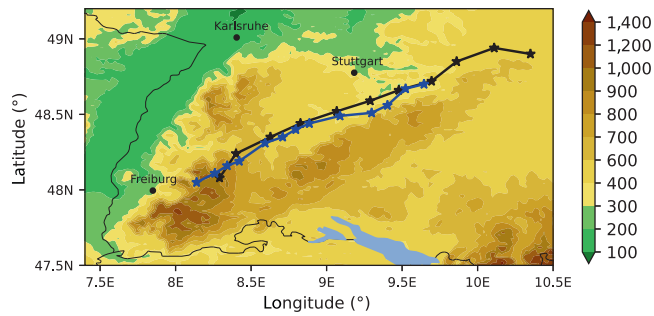


FIGURE 6 Observed (black) and simulated cell track of the 1 km run with the double-moment scheme and low CCNs concentration (1km_2MOM_low; blue) overlaid on the topography in meters above sea level. [Colour figure can be viewed at [wileyonlinelibrary.com](https://onlinelibrary.wiley.com)]

RADOLAN observations. For all scales ranging between 2 and 128 km analysed, the 1 km configuration with low CCNs concentration has the highest values, indicating better agreement with observations (not shown). The model run with operational settings (i.e., 2 km grid spacing and 1MOM scheme) has the largest error of all. The fact that the 2MOM runs at 2 km grid spacing perform better than the run with operational settings (i.e., 2 km grid spacing and 1MOM scheme) indicates the potential benefits of using a 2MOM scheme even if the storm of interest was not simulated at 2 km grid spacing.

We manually determined the cell tracks of the supercell storm in the radar-derived precipitation data and the model output by connecting the respective rain maxima from each available output time step. The cell track of the successful model run (1km_2MOM_low) shows remarkably good agreement with observations (Figure 6).

The lifetime is 6.5 hr, which is slightly shorter than observed. This is also related to the fact that, in the simulation, the storm has a time delay and merges with convection coming in from the south earlier in the evening. We decided not to add that to the lifetime of the supercell storm. Thus, the cell track is shorter, too (136 km).

The fact that supercells are more long-lived than non-supercell thunderstorms is due to both the persistent rotating updraught of a supercell, which enhances vertical motion, and to an updraught–downdraught configuration that generally prevents precipitation from falling through the updraught (e.g., Bunkers et al., 2006). The dynamical criterion instead of a longevity criterion for the classification of a storm as a supercell is the presence of a persistent, deep mesocyclone within the updraught (Markowski & Richardson, 2011). To check this dynamical criterion for the classification of the simulated storm as a supercell, we analysed midlevel wind fields for the convectively active time period. In the vicinity of the city of Rottenburg, the rotation of the storm can clearly be

identified in maps of wind components and streamlines for the period between 1600 and 1730 UTC (not shown). To better identify storm-scale rotation in our simulations, we calculated the updraught helicity by taking the vertical integral of vertical vorticity times the vertical velocity in the layer between 2 and 5 km above ground level (agl). We find values larger than $75 \text{ m}^2 \cdot \text{s}^{-2}$, which corresponds to a threshold of identifying and tracking supercells used by Ashley et al. (2023). These high values mark the rotating part of the supercell storm that lies ahead of the main precipitation area in the direction of storm propagation, providing a suitable updraught–downdraught configuration for the existence of a supercell storm, as mentioned earlier.

Although we apply the four different CCNs scenarios for two resolutions of the ICON model, the successful configuration (1km_2MOM_low) is still one single realization of the event and the good result could be coincidental. To provide more confidence in the robustness of this result, we performed additional simulations using the 2MOM scheme at the same grid spacing and changed the low CCNs concentration by $\pm 1\%$, $\pm 2\%$, and $\pm 3\%$. All of these runs produce a long-lived supercell storm in the area where the observed supercell occurred, with only minor differences in location and size. As will be shown later, the agreement between several observed variables and our successful model run gives us reason to believe that the good result is due to the right reason. To sum up, even if there is a temporal delay with respect to the observed precipitation, the combination of high-resolution model grid spacing and a 2MOM scheme with an assumed clean environment is able to successfully simulate the supercell storm of this day. We now focus on reasons for the different behaviours and, in particular, why only this combination produces a good hindcast of the event.

3.2 | Thermodynamic environment and convection-related parameters

As all model runs use the same initial and boundary data, the environmental conditions of the supercell storm are impacted by processes depending on the horizontal and vertical grid spacing and the different microphysical assumptions only. At the KITcube main observation site of Rottenburg, radiosoundings were launched by KIT between 0500 UTC and 2300 UTC in intervals ranging between 1.5 and 3 hr. To investigate the pre-convective environment, we now compare the 1230 UTC sounding (see Figure 4) with ICON profiles at the nearest model grid point to the radiosonde station (Table 3). We used the Python tool MetPy (May et al., 2022) to calculate the convective indices for both the

TABLE 3 Convective indices for the radiosonde ascent at Rottenburg (1230 UTC) and for simulated profiles at the corresponding model grid point.

Run	CAPE ($\text{J}\cdot\text{kg}^{-1}$)	CIN ($\text{J}\cdot\text{kg}^{-1}$)	BRN
obs	469	11	22
2km_1MOM	135	22	6
2km_2MOM_low	234	37	16
2km_2MOM_int	199	24	13
2km_2MOM_high	62	67	4
2km_2MOM_vhigh	64	78	5
1km_1MOM	248	24	8
1km_2MOM_low	515	12	18
1km_2MOM_int	704	0	30
1km_2MOM_high	540	25	26
1km_2MOM_vhigh	702	3	27

Note: Calculations were done using a parcel consisting of mean-layer values of temperature and moisture from the lowest 50 hPa. BRN, bulk Richardson number; CAPE, convective available potential energy; CIN, convective inhibition.

observational data and the model output to ensure the comparability of the results. The radiosounding revealed a mean-layer CAPE (i.e., averaged over the lowest 50 hPa) of $469 \text{ J}\cdot\text{kg}^{-1}$, a CIN of $11 \text{ J}\cdot\text{kg}^{-1}$, and a BRN of 22. Four of the model runs show BRN numbers less than 10, which indicates that the shear may be too strong given the weak buoyancy to develop sustained convective updraughts. The different model configurations produce a wide range of CAPE values between 62 and $702 \text{ J}\cdot\text{kg}^{-1}$, and CIN also shows a large spread ($0\text{--}78 \text{ J}\cdot\text{kg}^{-1}$). Our best model result presented in the last section (i.e., the 1 km run with 2MOM scheme and low CCNs concentration) shows the best agreement with all these convective indices derived from radiosonde data (CAPE = $515 \text{ J}\cdot\text{kg}^{-1}$; CIN = $12 \text{ J}\cdot\text{kg}^{-1}$; BRN = 18). Although many other parameters also need to be assessed, this good agreement makes us believe that the good model result is due to the right reason. Interestingly, all CAPE values from the runs with 1 km grid spacing are higher than their corresponding run at coarser resolution. This will now be assessed with the analysis of spatial averages of convection-related parameters over the MOSES domain.

The radiation balance at the ground shows higher maximum values for the 1 km simulations (Figure 7a). This is due to the fact that slightly less low-level and mid-level clouds are simulated with finer resolution before noon (not shown). The difference between the largest ($486 \text{ W}\cdot\text{m}^{-2}$) and smallest ($413 \text{ W}\cdot\text{m}^{-2}$) daily maximum is quite high at $73 \text{ W}\cdot\text{m}^{-2}$, which has implications on the surface energy budget. Both 1 km runs with high and very high CCNs concentration reveal a slightly stronger increase in CAPE in the morning hours with a maximum between 1430 and

1500 UTC (Figure 7b). All remaining model runs reach their maximum CAPE values around 1800 UTC, which coincides with the maximum of 2 m specific humidity (not shown). For the initiation of deep convection, not only is the existence of CAPE important, but also CIN has to be overcome. Therefore, regions with sufficient amounts of CAPE need to have low values of CIN or require a strong trigger mechanism. We determined the number of grid points for which both of the following conditions are met: (a) CAPE larger than $600 \text{ J}\cdot\text{kg}^{-1}$ and (b) CIN less than $5 \text{ J}\cdot\text{kg}^{-1}$. Our model runs show that a large fraction of the grid points (43–76%) in the MOSES region fulfil this criterion between 1200 UTC and 1700 UTC (Figure 7c). Again, the 1 km runs show a stronger increase in the morning hours than the 2 km runs do. Except for the fact that the higher resolution runs usually reach their maximum values earlier, the maximum values show only a little sensitivity to the model grid spacing. Instead, the dependence on the assumed CCNs concentration is much stronger. The lowest percentage of grid points meeting this criterion occurs in clean environments, with an almost systematic increase with higher CCNs concentrations. Another systematic difference between the two grid spacings applied for this case study is the fact that low-level wind convergence is much stronger at finer resolution (Figure 7d). For the latter, on the contrary, the response to different CCNs concentrations is much smaller than the grid spacing effect. As wind convergence is connected to ascending air parcels, systematic stronger updraught velocities in the planetary boundary layer are simulated with 1 km grid spacing (Figure 7e). There is an almost linear relationship between low-level wind convergence and lifting of air

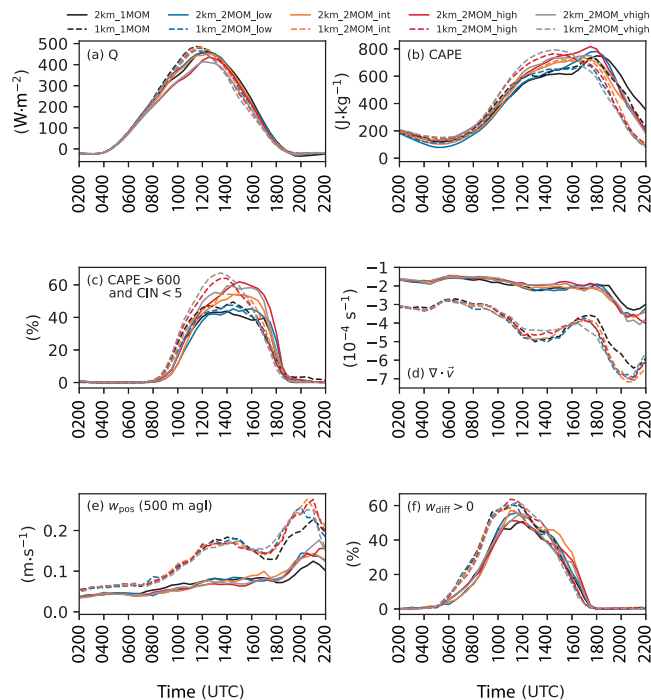


FIGURE 7 Time series of spatial averages of surface radiation budget (Q), convective available potential energy (CAPE), fraction of grid points with CAPE larger than $600 \text{ J}\cdot\text{kg}^{-1}$ and convective inhibition (CIN) less than $5 \text{ J}\cdot\text{kg}^{-1}$, 10 m wind divergence, upward velocity at 500 m above ground level (agl) w_{pos} , and fraction of grid points with $w_{\text{diff}} > 0 \text{ m}\cdot\text{s}^{-1}$. See further explanations in the text. [Colour figure can be viewed at wileyonlinelibrary.com]

parcels as a consequence of mass continuity: the stronger the wind convergence, the higher are the vertical velocities. Stronger updraughts at finer grid resolution were also found in previous studies (e.g., Barthlott & Davolio, 2016; Donner et al., 2016). Another measure for the likelihood of deep moist convection is the velocity difference w_{diff} , defined as (e.g., Schneider et al., 2018)

$$w_{\text{diff}} = w_{\text{max}} - w_{\text{CIN}}, \quad (1)$$

with w_{max} the simulated maximum vertical velocity below the LFC and $w_{\text{CIN}} = (2 \times \text{CIN})^{1/2}$ being the updraught required to overcome CIN. A positive value of w_{diff} indicates that the lifting of air parcels is strong enough to overcome CIN. These air parcels can reach their respective LFC and initiate convection if sufficient CAPE is present. The 1 km simulations reveal a stronger increase in the number of grid points with positive w_{diff} and also larger maxima than the 2 km runs (Figure 7f). The overall good conditions for the development of deep convection are demonstrated by the relatively high fraction of grid points fulfilling this criterion ranging between 51% and 63%.

Interestingly, different CCNs concentrations only have a weak impact on low-level wind convergence, PBL

updraughts, and the velocity difference w_{diff} , whereas changing the grid spacing affected those variables significantly. In contrast to this, CAPE and the combined measure of coinciding high CAPE and low CIN are more sensitive to aerosols than model grid spacing is. A number of recent studies have shown that there is an almost linear relationship between CAPE and low-level equivalent potential temperature θ_e (e.g., Kohler et al., 2010). In the polluted model runs, domain-averaged θ_e values are slightly higher than in clean conditions because there are less clouds and also less precipitation in the morning (not shown). In addition, CIN is lower in the polluted simulations. Furthermore, temperature lapse rates tend to increase with pollution as well, most probably related to the different release of latent heat during cloud formation. All these effects combine to have a positive aerosol impact on CAPE availability and suitability for convection on the day of investigation.

The analysis of these convection-related parameters has shown that the environmental conditions for deep moist convection are generally met by all model runs, and most of the finer resolved simulations show even more suitable conditions. However, the only model run to simulate the supercell storm of this day (i.e., $1 \text{ km}_2\text{MOM}_{\text{low}}$) does not show the best conditions of all model runs. For example, CAPE values of this run are among the lowest of all 1 km simulations, and the percentage of grid points with high CAPE and low CIN is one of the lowest of all model runs. It is also worth noting that the 1 km run with the 1MOM scheme leads to similar thermodynamic conditions as the successful 2MOM run assuming clean conditions at the same resolution. Even though the supercell was not simulated with the 1MOM scheme, there were overall improvements with respect to surface precipitation (see Figure 5), which points to the potential benefits of finer resolution for operational weather forecasting.

3.3 | Aerosol measurements

The simulation results have shown that, of the main set of runs tested (Table 2), only the 1 km run using the 2MOM scheme with a low CCNs concentration of 100 cm^{-3} was able to simulate the supercell storm passing over the main site of Rottenburg. During the Swabian MOSES field campaign, aerosol particle concentrations and size distributions were measured continuously from June until August 2021 with an optical particle counter (Fidas 200 E) at 3.7 m agl at the Rottenburg station. The measurement range of this instrument spans between 0.18 and $18 \mu\text{m}$ and is distributed over 64 channels. The temporal resolution is 1 min . For our analysis we selected data from the bins between 0.18 and $1.2 \mu\text{m}$, which roughly represent the

average diameter of the main aerosol contributors to CCNs concentrations over Germany (e.g., Hande et al., 2016). Other aerosol measurements including for example concentrations of ice nucleating particles and spatial aerosol distributions (scanning aerosol lidar) were conducted as well; for an overview, see (Kunz et al., 2022).

For each day in June, we selected aerosol data of the pre-convective environment for a period of 1.5 hr and computed a temporal average value. The resulting time series is given in Figure 8. It can be seen that June 23 (marked by the grey dashed line) is the day with the lowest potential CCNs concentration of the entire month. The value of 100 particles/cm³ corresponds to the one that the ICON model is assuming in clean conditions. Of course, it must be stated that these observations are coming from one single instrument operating near ground level. However, aerosol lidar and ceilometer measurements show an increasing aerosol backscatter with increasing altitude during the day at the Rottenburg station in cloud-free periods until about 1 hr before the supercell storm passage; see (fig. 5, Kunz et al., 2022). This is in line with the evolution of the boundary layer. There are also some peak backscatter values at cloud levels, which may be due to pre-activated aerosol particles at altitudes where clouds form. Based on radiosonde humidity profiles and an assumed hygroscopic growth of the aerosol particles, backscatter coefficients of dry aerosol particles were estimated, making the backscatter data at different altitudes better comparable. We found that the relatively low backscatter values near the ground level are thus very similar to those near cloud level. Hence, the potential CCNs concentrations were relatively low

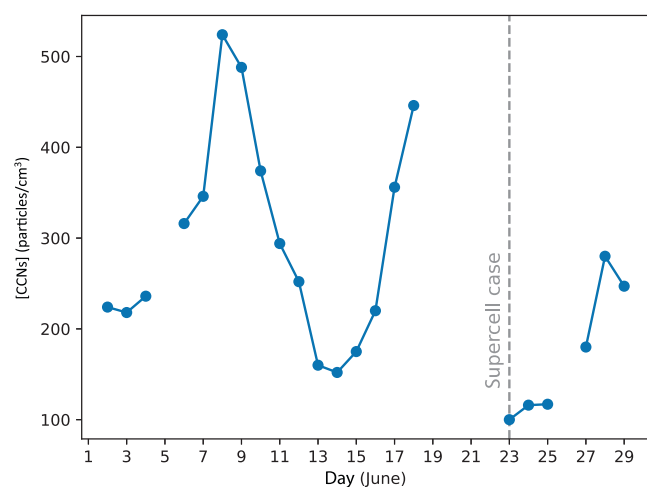


FIGURE 8 Mean cloud condensation nuclei (CCNs) concentration in the pre-convective environment at the station of Rottenburg for the month of June. Gaps indicate periods for which data are not available. The day of the supercell studied here is represented by the grey dashed line. [Colour figure can be viewed at [wileyonlinelibrary.com](https://onlinelibrary.wiley.com)]

near ground level but also at cloud level. This becomes evident when compared with the backscatter profile from June 21 for a similar time of the day, which shows significantly higher values caused by a Saharan dust plume (not shown). The case of June 23 is clearly characterized by the lowest potential CCNs values of the month, which indicates that the low aerosol concentration in the successful model run is a meaningful assumption for this case.

3.4 | Supercell passage over observation stations

3.4.1 | Surface meteorological station

One important aspect of this work is the fact that the supercell storm passed directly over the main observational site at Rottenburg and the surrounding hail sensors. This allows us to compare, among other things, the effects of the supercell storm on meteorological variables at the surface. As observed by a meteorological energy balance station, the passage of the supercell led to a strong temperature decrease of 11 K between 1420 UTC and 1610 UTC (not shown). Averaged over a 10-min period, the maximum wind speeds reached 7.0 m·s⁻¹ and relative humidity increased from 56% to 97%. By extracting the data from the nearest model grid point, the successful model run at 1 km grid spacing with low CCNs concentration shows similar changes: a temperature decrease of 12 K, an increase in mean wind speed to 7.6 m·s⁻¹, and an increase in relative humidity from 60% to 99%. The time frame in which these alterations occurred in the simulations, however, is 1 hr, and thus shorter than observed. This indicates that either (a) the propagation speed of the simulated supercell was higher than observed or (b) simulated rain rates and the associated cold pool are both stronger than observed or that both aspects (a) and (b) are the case, as shown later herein. The propagation speeds of simulated and observed storm were derived from the cell tracks. It turns out that the passage of the simulated cell over the Rottenburg site is faster (8.9 m·s⁻¹) than of the observed one (7.6 m·s⁻¹). Moreover, maximum rain intensities in the ICON model are slightly higher (18.8 mm/30 min) than measured by two ombrometers on site (13.5 and 16.9 mm/30 min).

3.4.2 | Hail monitoring system

Eight surface stations in the Swabian MOSES area were additionally equipped with the automatic hail monitoring system HailSens from Hyquest Solutions. These stations were placed at locations most frequently affected by hail based on analyses of long-term radar data (Puskeiler

et al., 2016). If a falling hailstone hits the measurement plate of about 0.2 m^2 in size, the plate's vibration is recorded using a piezoelectric microphone. The signal of each hailstone is converted into kinetic energy and hail diameter is automatically sent to a web interface.

On June 23, five of the eight hail sensors recorded maximum hail sizes of 2 cm from the supercell that passed over the main site of Rottenburg earlier on the same day (Kunz et al., 2022). The highest number of hailstones was recorded at the Großbettlingen station (about 30 km north-east of Rottenburg), with a total of 1,132 hailstones in just 13 min and an average diameter of about 1 cm. The Mittelstadt sensor, located 6 km southwest of Großbettlingen, recorded 486 stones, with an average diameter of about 8 mm, a few minutes earlier. For the intercomparison with ICON, we computed hail size distributions from the predicted mass and number densities at the lowest model level; see (app. A, Seifert & Beheng, 2006). This was done in 30-min intervals for all grid points inside a rectangular box with a size of $0.6^\circ \times 0.6^\circ$ surrounding the supercell storm. At the time of the passage of the simulated storm in the successful model run, the modal value of the hail size distribution (i.e., the particle size most commonly found in the distribution) lies at a diameter of 7.8 mm (not shown), which fits the observations well. As the maximum particle mass x for hail in the ICON model is restricted to 5.4×10^{-4} kg, the power law for the diameter $D(x) = 0.1366x^{1/3}$ gives a highest possible hail diameter of 11 mm. The computed hail size distributions, however, are not zero at the upper end of the size spectrum, but rather lie at 60–80% of the highest value of the respective distribution. This indicates that larger hail stones are probable, even if they cannot be simulated with the present range of allowed particle mass.

In addition, we calculated mean hail number fluxes averaged over the same rectangular box surrounding the supercell storm. As the supercell storm is later than observed, we shifted the time of the observations to match its later occurrence in the ICON model. The storm hit the city of Großbettlingen at 1900 UTC, and the mean hail number fluxes calculated from 1-min averages are $6.7\text{ m}^{-2}\cdot\text{s}^{-1}$ for Großbettlingen and $3.3\text{ m}^{-2}\cdot\text{s}^{-1}$ for Mittelstadt. The value for the successful ICON run lies in between these two values (Figure 9), which again confirms the adequate simulation of the supercell storm from that day.

To get information on hail occurrence over a large area, we combined the two operational C-band radars from DWD located at the Feldberg and Türkheim with the KIT C-band and X-band radars to provide a unique radar composite in that area (see Figure 10 for their locations).

Using a reflectivity threshold of 57 dBZ as a proxy for hail at the ground, the supercell storm produced first

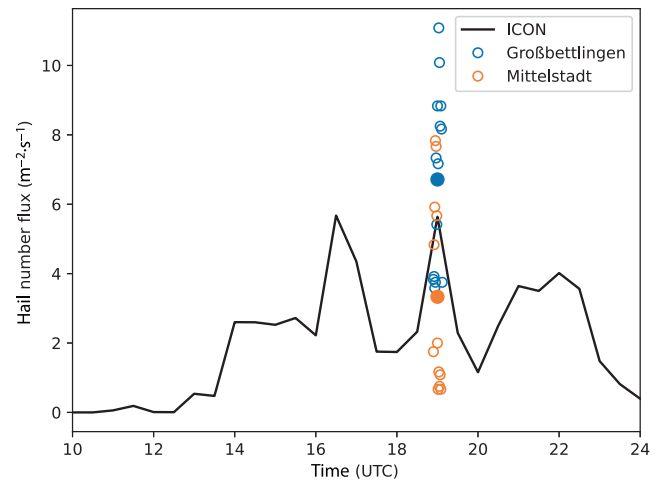
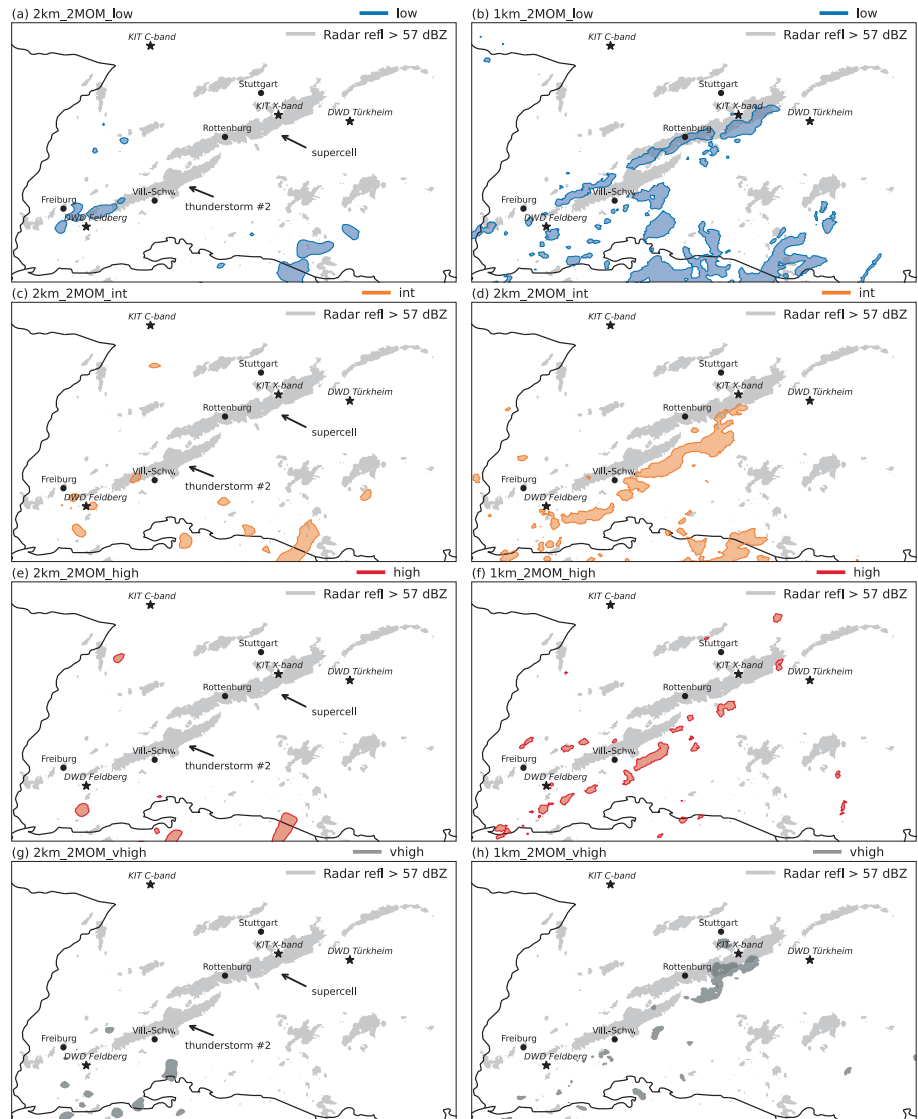


FIGURE 9 Simulated and observed hail number fluxes. Open circles represent hail observations with 1 min temporal resolution for the observational sites in Großbettlingen (blue) and Mittelstadt (orange). Filled circles indicate mean values for these time periods. Model results represent the mean hail surface flux in a box following the cell track. [Colour figure can be viewed at wileyonlinelibrary.com]

hail at 1330 UTC to the north of Villingen-Schwenningen (Figure 10). Later on, an approximately 10-km wide corridor of larger reflectivities formed as the storm propagated towards the northeast. The second thunderstorm, which was initiated later (see Figure 3b), also produced large amounts of hail but had a shorter lifetime than the supercell storm passing over the Rottenburg site. These two different features have been annotated in Figure 10a for easier distinction. Owing to the missing supercell storm at 2 km grid spacing, there is very little hail in the southern part of the domain and some isolated small areas over the northern Black Forest. With the decreased grid length of 1 km (Figure 10b) there is significantly more hail at the ground than at coarser resolution. Total hail amounts are largest for low CCNs concentration and decrease with increasing CCNs concentration (Figure 10c–h), a feature also found in previous work (e.g., Barrett & Hoose, 2023; Barthlott et al., 2022b). The percentage decrease is quite large, with 46% at 2 km and 67% at 1 km grid spacing. At the finer grid resolution, the large spread in hail accumulations is also obvious from their spatial occurrence and timing (Figure 10b). The runs with low and intermediate CCNs concentrations show an increase in hail amounts already from 1400 UTC, whereas the more polluted scenarios have a much weaker increase (not shown). The largest increase in hail is simulated in the evening when the convective cells move into the MOSES domain from the south, again with a temporal delay and weaker intensity for the polluted cases. From the comparison with the radar reflectivity it is evident that only the model run assuming a low

FIGURE 10 Maximum radar reflectivity larger than 57 dBZ based on data from four radars integrated between 1200 and 2000 UTC (grey shaded) and ICON-simulated hail amounts larger than 3 mm for (a, c, e, g) 2 km grid spacing and (b, d, f, h) 1 km grid spacing for the same period. [Colour figure can be viewed at wileyonlinelibrary.com]



CCNs concentration shows a good agreement with respect to the spatial occurrence of hail. Thus, the good representation of the supercell storm is not only evident from total precipitation amounts, but also from the hail that can only be simulated using the 2MOM scheme instead of the operational 1MOM scheme.

3.4.3 | Wind lidar

The main measurement site in Rottenburg was equipped with a WLS200s Doppler wind lidar, which allows for continuous measurements of the wind profile above. Wind profile retrieval requires sufficient presence of scatterers (aerosol; e.g., dust, pollen). A retrieval is regularly possible from 50 m up to the boundary layer/residual layer height and sometimes also above. The lidar operated at 25 m range resolution and conducted a Doppler-beam-swinging

scan pattern at 60° elevation (four orthogonal azimuth directions stares and one zenith stare). The accumulation time at the stare positions was set to 5 s, resulting in a total duration of the scan pattern of 41 s, including slew time. Quality control of the raw radial velocity measurements includes signal-to-noise-ratio filtering and removal of second-trip echoes due to range ambiguity. The wind profile retrieval is conducted based on aggregation and median filtering of the quality-processed radial velocities in 10 min intervals. The vertical wind measurements (determined from the zenith stare) may be compromised if rain is present, since the Doppler peak of the rain droplets overwhelms that of the aerosol. In this case, the vertical velocity of the droplets is measured and not the vertical wind.

Prior to the supercell passage, winds in the boundary layer were predominantly from north to easterly direction with wind speeds below 5 m s^{-1} (Figure 11a). Above the

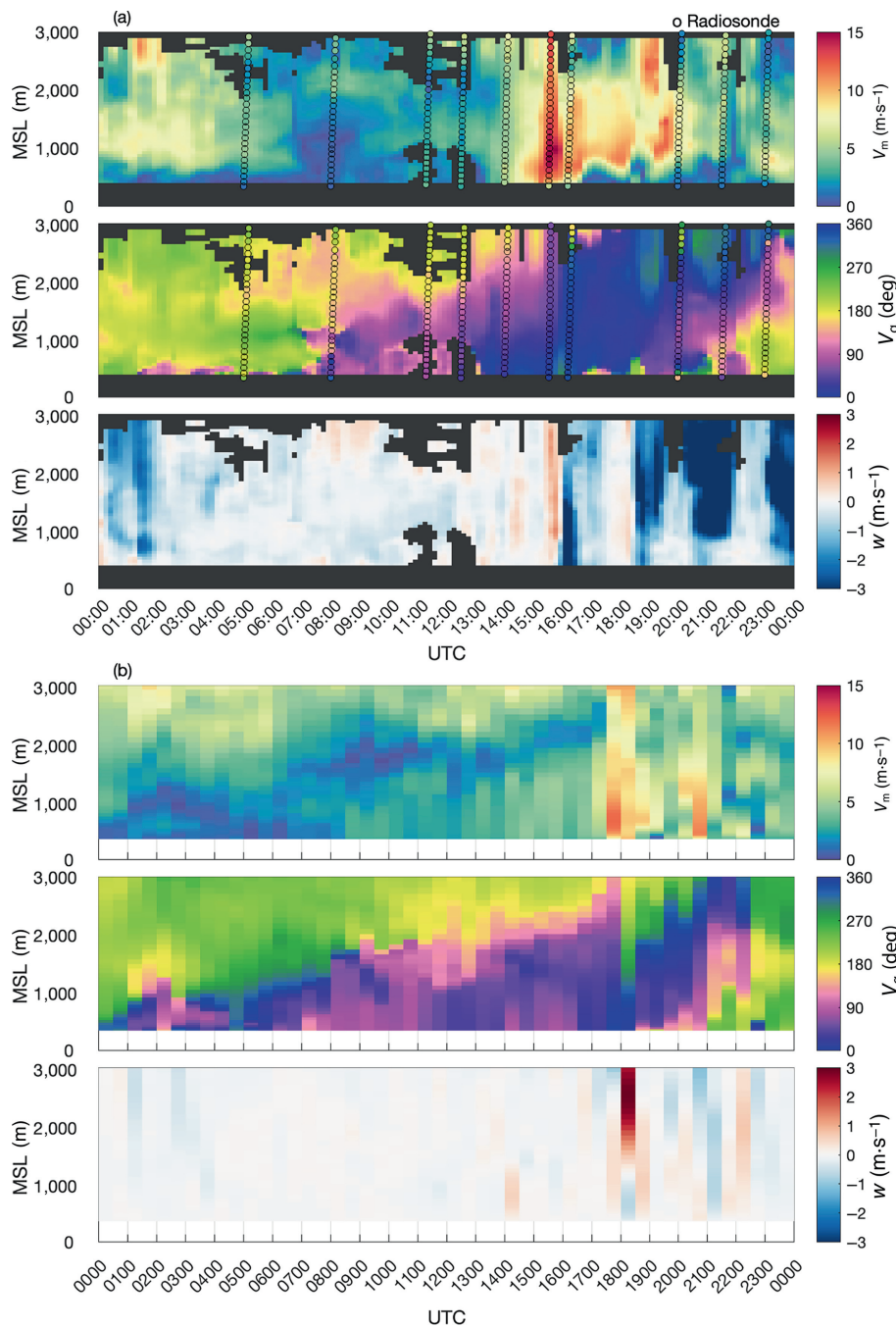


FIGURE 11 Wind speed, wind direction, and vertical wind from lidar and radiosonde observations at (a) Rottenburg and (b) from run 1km_2MOM_low. MSL: mean sea level. [Colour figure can be viewed at wileyonlinelibrary.com]

boundary layer, a southwesterly flow prevailed. In the lowest 500 m agl, the approach of the supercell induced a wind veer towards northerly directions and a strengthened inflow around $5 \text{ m}\cdot\text{s}^{-1}$. The passage of the supercell at 1600 UTC produced wind speeds up to $15 \text{ m}\cdot\text{s}^{-1}$ from north to westerly directions, measured in agreement by wind lidar and radiosonde (despite the inevitable position differences due to the drift of the radiosonde). Flow after the passage remained from northerly directions up to 2,000 m agl.

We extracted wind profiles from the runs using 2MOM schemes and a low CCNs concentration by selecting the data at the nearest grid point to the lidar station.

Confirming the previous analyses, the wind profile evolution produced by the 1km_2MOM_low run shows the best agreement of all model realizations of this case (Figure 11b). This model run captures a number of prominent features associated with the passage of the supercell, whereas the 2km_2MOM_low run, for example, does not. Examples include the turning of the inflow and the strong increase in wind from northwesterly directions during passage of the cell (2 hr delayed in the model). The 2km_2MOM_low run is not able to produce a similar signature in the wind signal (not shown). As expected, comparison with measurements still shows

some differences, even for the 1km_2MOM_low run. Most prominently, the strong and deep northerly flow after passage of the supercell is not simulated; instead, the model simulates westerly flow. A comparison of all runs confirms that the 1km_2MOM_low run produces the strongest wind maximum associated with the passage of the supercell at all altitudes (not shown). The second-best run is the 1km_2MOM_vhigh run, which also produces a maximum, but with reduced strength and extended duration. This run, however, did not simulate the supercell storm adequately. Instead, the convection was initiated more to the north, later than observed, and took a different path (see also explanations in Section 3.1). All other runs do not produce a wind speed maximum of comparable magnitude; the 2 km runs generally do not produce maxima.

3.5 | Cloud tracking

In order to further analyse the convective development in the simulations, we use version 1.4.2 of the Python package *tobac* (Tracking and Object-Based Analysis of Clouds) (Heikenfeld et al., 2019). The *tobac* software package is used for identifying, tracking, and analysing clouds and other meteorological phenomena in different types of gridded datasets. It is set up in a modular way to include different algorithms for feature identification, tracking, and analyses. In this study, we use precipitation rates at high temporal resolution (5 min) to track convective clouds between 0300 UTC and 2400 UTC that have a minimum lifetime of 30 min. The tracking algorithm tracks individual convective cells and their volume by using a lower threshold of $5 \text{ mm} \cdot \text{h}^{-1}$.

As can be seen in Figure 12, the 1 km simulations generate more than twice as many convective cells as the 2 km simulations do. In most of the model runs the shorter cell tracks are located over eastern France, the Rhine Valley, and also the Black Forest, whereas the longer cell tracks occur more in the east and southeast of the MOSES domain. The number of detected cells (depicted at the top right corner of each panel in Figure 12) in runs using a 1MOM scheme is similar to the number of cells in runs using the 2MOM scheme and assuming a clean environment. As the CCNs concentration increases, the number of cells decreases in both model resolutions. The decline is very strong at about 46% (2 km) and 53% (1 km) and demonstrates the important impact of aerosol–cloud interactions for quantitative precipitation forecasting. The negative aerosol effect on convective clouds and precipitation found here is in agreement with previous studies investigating multiple cases under different synoptic controls using the ICON model (Barthlott et al., 2022a, 2022b). These results should not be considered

universally valid, as other studies have reported positive aerosol effects (e.g., convection invigoration theory; Rosenfeld et al., 2008). However, the validity of the invigoration hypothesis remains open because of contradictory results depending on the details of the microphysics scheme, the environmental conditions, or the cloud type (e.g., Altaratz et al., 2014; Fan et al., 2017; van den Heever et al., 2011). The large variability in simulated cell tracks is particularly important for flood forecasting because the precipitation location and intensity are crucial for predicting the amount of precipitation in individual river catchments.

In addition to the trajectories, *tobac* also assesses the lifetime of the detected cells. Distributions of these lifetimes from all model runs are shown in Figure 13. Consistent with the larger number of detected cells at higher grid spacing shown in Figure 12, in almost every lifetime class there are more cells at 1 km grid spacing than their respective counterpart at 2 km grid spacing. The absolute increase is largest for the shortest lifetimes. For lifetimes longer than 150 min there are only minor variations present, indicating that the model resolution only has a small effect on long-lived convective storms in an environment with suitable wind shear. Moreover, the general form of the distribution does not change with model grid spacing, and most cells are detected at short lifetimes. The CCNs influence is evident from (a) reduced number of detected cells and (b) shorter cell lifetimes in the majority of classes.

3.6 | Grid spacing effects on convection initiation

The results of the set of simulations tested here have shown that a successful simulation of the supercell storm can only be achieved with high model grid resolution and an aerosol-aware microphysics scheme assuming a low CCNs concentration. It is now of interest to analyse what differences exist in convection initiation when comparing only the two model runs assuming a low CCNs concentration (i.e., runs 2km_2MOM_low and 1km_2MOM_low). The analysis of domain averages of convection-related parameters in Figure 7 showed that CAPE is rather similar in both configurations and only a slightly higher fraction of grid points with large CAPE and low CIN exist at 1 km grid spacing. Low-level wind convergence (i.e., the mean convergent contribution to wind divergence), however, is much stronger at finer resolution, and the induced updraughts in the PBL are, on average, twice as large at 1 km grid spacing than with coarser resolution around noon. Differences in the simulations are now further highlighted by examining maps of CAPE, low-level winds,

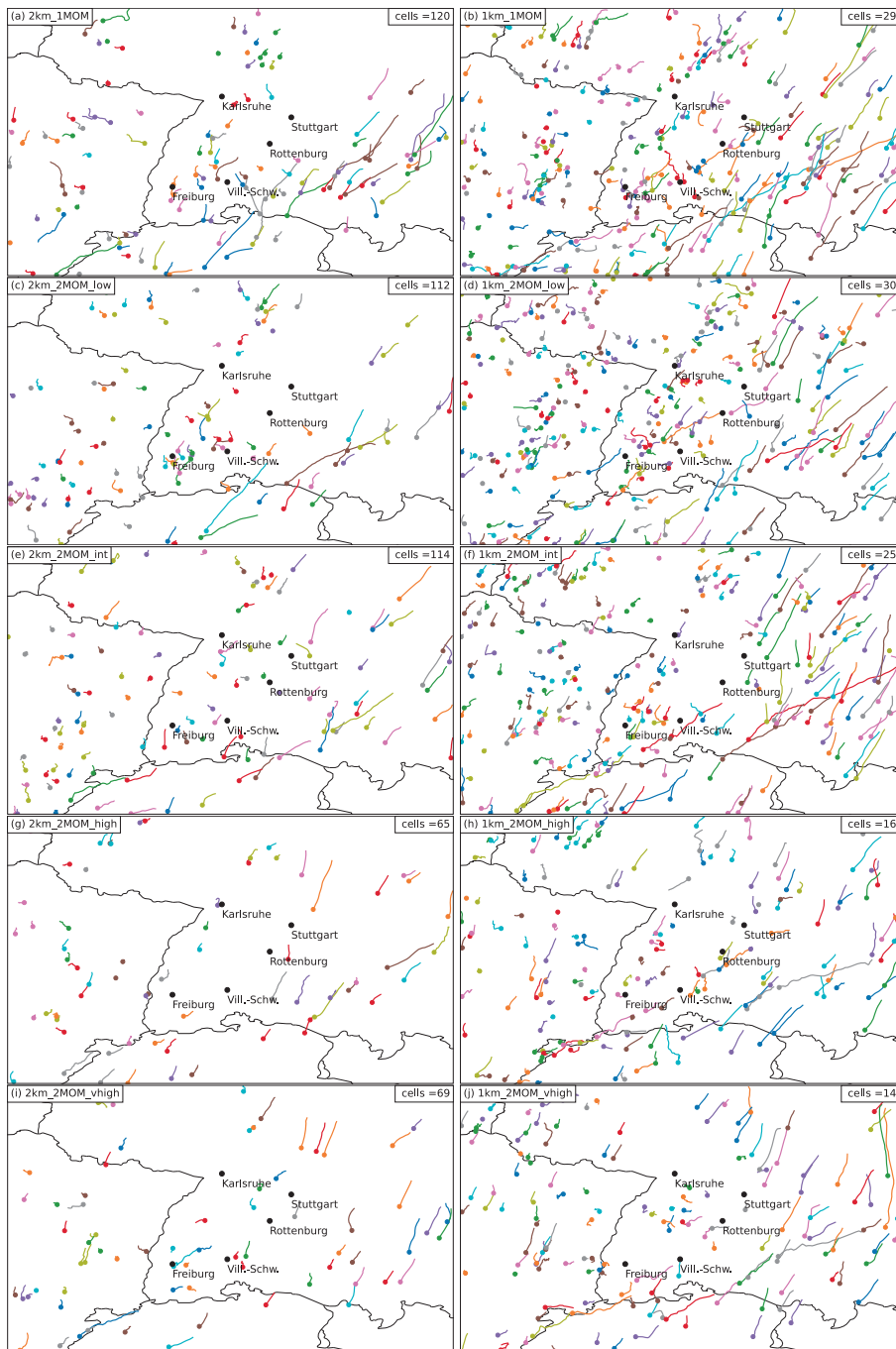


FIGURE 12 Tracks of convective clouds for (a, c, e, g, i) 2 km and (b, d, f, h, j) 1 km grid spacing from 0300 UTC to 2400 UTC. Filled circles indicate the point of first detection. [Colour figure can be viewed at wileyonlinelibrary.com]

and precipitation between 1200 and 1500 UTC for both resolutions for the southern Black Forest area, where the initial cells developed (Figure 14).

At 2 km grid spacing, there is an approximately four times larger convective cell to the north of the city of Freiburg than in the 1 km simulation at 1230 UTC. This cell produced convective precipitation already at 1030 UTC. At the same time, the 1 km run initiated convective precipitation more to the north, which allowed the transport of moist and warm air towards the crests of the southern Black Forest. This led to a tongue of high

CAPE being present at finer resolution east of Freiburg at 1230 UTC (Figure 14b). This is also demonstrated by the fact that integrated over a rectangular box over the southern Black Forest only (depicted by the black rectangle in Figure 14a), 60% of grid points at 1 km grid spacing had suitable conditions for the development of deep convection (CAPE larger than $600 \text{ J} \cdot \text{kg}^{-1}$ and CIN less than $5 \text{ J} \cdot \text{kg}^{-1}$), whereas only 48% of grid points at coarser resolution fulfilled these criteria. Resulting from low-level wind convergence and associated lifting of air parcels, convection was initiated 30 min later southeast of

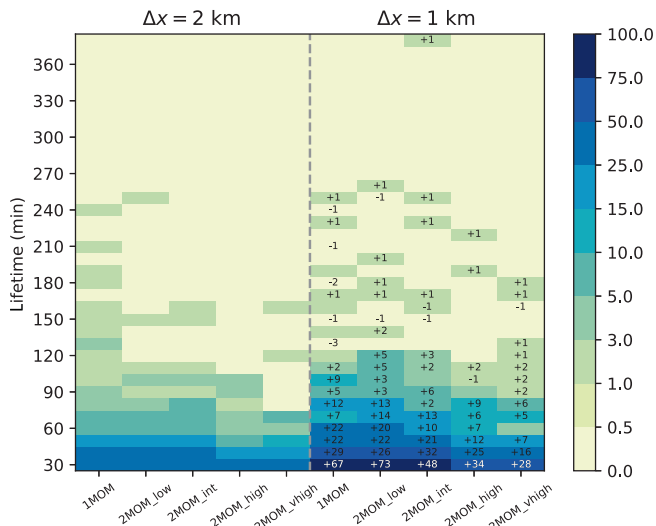


FIGURE 13 Lifetime of tracked convective clouds. Numbers indicate the differences of the number of cells in each lifetime class simulated with 1 km grid spacing to their respective counterpart at 2 km. [Colour figure can be viewed at [wileyonlinelibrary.com](https://onlinelibrary.wiley.com)]

Freiburg in both model runs. CIN was very low ($<1 \text{ J}\cdot\text{kg}^{-1}$) in that area in both configurations (not shown). At finer grid resolution (Figure 14d,f), the convection is much more intense and the convective complex is much larger, favoured by the higher CAPE values. The smaller cell at 2 km grid spacing produces weaker rain intensities than the one at 1 km does (Figure 14c) and starts to decay after 1400 UTC (Figure 14e,g,i) until it is completely dissolved at 1530 UTC. The weaker CAPE, but also stronger impact of entrainment due to the small cell size, is supposed to be the reason for the short lifetime. At 1 km grid spacing, however, the larger complex is able to intensify and produces over 40 mm/30 min in its core between Freiburg and Villingen-Schwenningen at 1430 UTC and 1500 UTC (Figure 14h,j). The cell then moves in a northeasterly direction, as already depicted by the cell tracks in Figure 6. We conclude that, on that specific day, the impact of model grid spacing leads to differences in the location and size of earlier convection which impacted the availability of CAPE in the region where the precursors of the supercell formed. The two impacts on CAPE were (a) consumption due to different convective coverage and intensity and (b) different strength of warm and moist air transport from the Rhine Valley towards the crest of the southern Black Forest.

One open question remains, namely whether an even finer model resolution would bring improvements. We therefore performed a model run with a horizontal grid spacing of 500 m and assuming a low CCNs concentration. With this setting, the model did not simulate a long-lived supercell storm like the corresponding run with 1 km grid

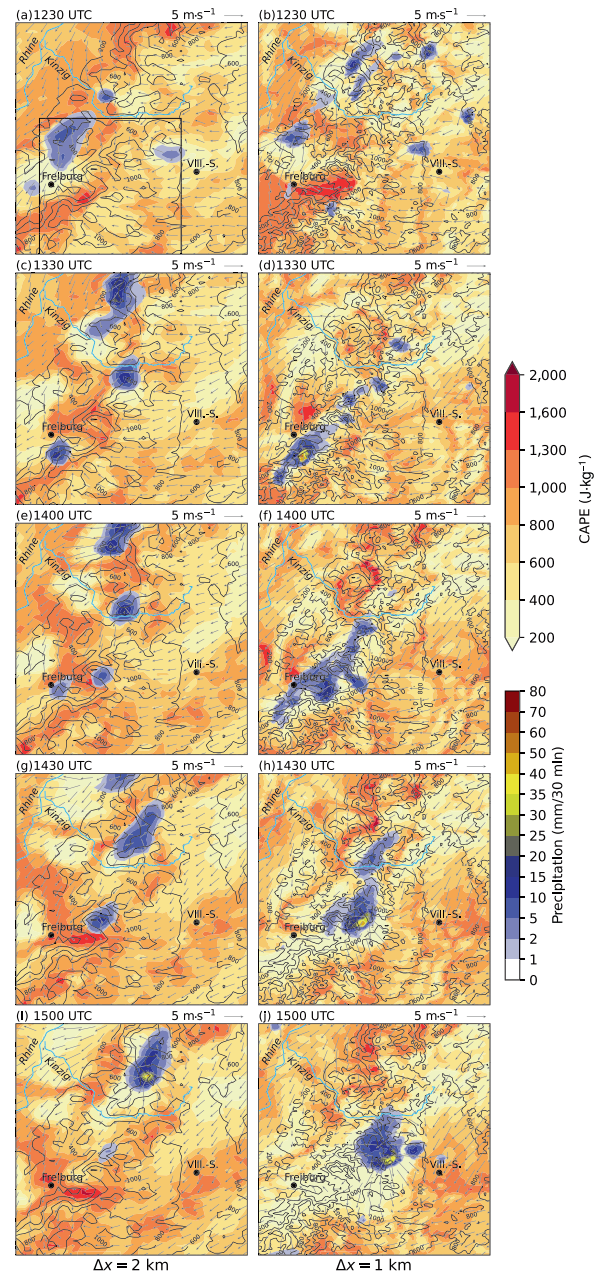


FIGURE 14 Mean-level convective available potential energy (CAPE), 30-min precipitation rates, and 10-m wind arrows for low cloud condensation nuclei concentration at (a, c, e, g, i) 2 km grid spacing (2km_2MOM_low) and (b, d, f, h, j) 1 km grid spacing (1km_2MOM_low). Surface elevation above sea level (m) is represented by black contour lines. [Colour figure can be viewed at [wileyonlinelibrary.com](https://onlinelibrary.wiley.com)]

spacing; instead, more small-scale convective cells were simulated (not shown). However, the convection initiation in this run occurs at a similar location and time, but the convection decays too quickly because the cell size is smaller than at 1 km grid spacing, and likely the entrainment shortens their lifetime. A grid spacing of 500 m is still above the large-eddy simulation limit (energy-containing

turbulence resolved), but it is still unclear whether a one-dimensional (used here) or a three-dimensional turbulence closure should be used. Further grid refinement tests, however, are beyond the scope of the present study.

3.7 | Aerosol–cloud interactions

As presented in the previous sections, there is a large influence of the assumed CCNs concentration on convective development in general and, in particular, on the supercell storm. For example, we found a large variability due to different CCNs concentrations in the number and lifetime of simulated cells using the cloud-tracking algorithm (Figures 12 and 13). Earlier results with the ICON model for convective situations in central Europe revealed a systematic precipitation decrease with increasing CCNs concentrations, at least when averaged over large domains such as Germany (e.g., Barthlott et al., 2022b). It is up to now unclear if this behaviour holds true for individual thunderstorms in complex terrain and to what extent the cloud type or the environmental conditions (e.g., wind shear, relative humidity) control the magnitude and sign of aerosol–cloud–precipitation interactions. We therefore apply the same Rainwater budget B analysis as in Barthlott et al. (2022b), which consists of the sources autoconversion (AC), accretion (ACC), melting (MELT), and sinks from evaporation (EVAP), riming (RIM), and rain freezing (FR) as follows:

$$B = AC + ACC + MELT - EVAP - RIM - FR. \quad (2)$$

We compute this budget analysis with spatial averages of vertical integrated microphysical process rates in the MOSES domain. To only investigate the time frame of the supercell storm, we need to neglect the larger scale convective systems moving in from the south in the evening. Thus, we restrict this analysis to time-integrated process rates until 1800 UTC. The analysis reveals a strong systematic decrease of the budget with increasing CCNs concentration at 2 km and 1 km grid spacings (Figure 15a).

The cold-rain processes dominate the rainwater production, as melting has the largest contribution (always larger than 60%). Autoconversion contributes only marginally to the warm-rain process and is only visible at low CCNs concentrations. The warm-rain process decreases both in magnitude and in terms of its contribution due to a reduced collision–coalescence process with increasing CCNs concentration. At a grid spacing of 1 km, there is an increase in the role of the cold-rain processes accompanied with a reduced warm-rain process, whereas the relative contributions do not change a lot at 2 km grid spacing but nevertheless show a stronger cold-rain process

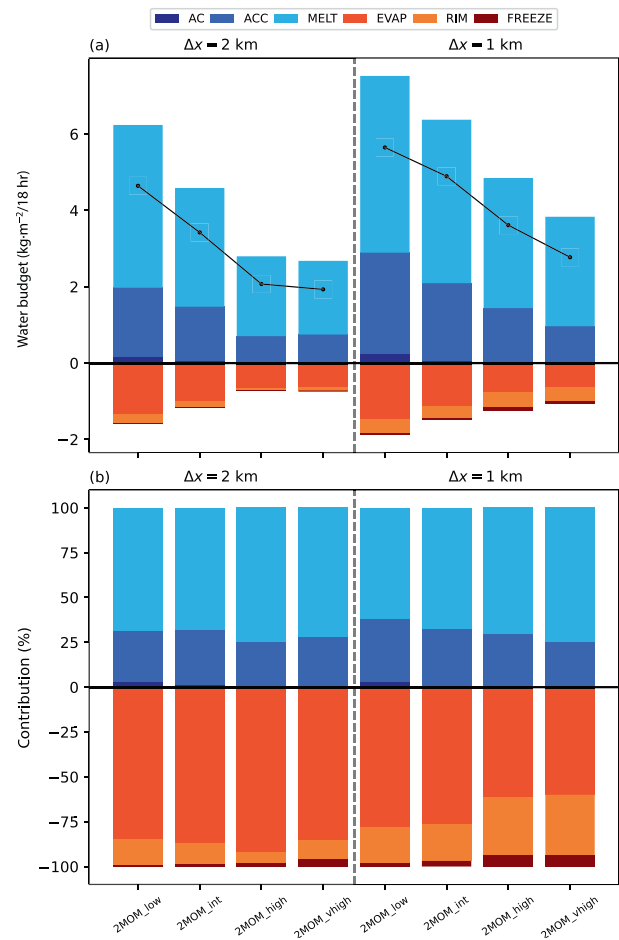


FIGURE 15 Rainwater budget: (a) with sources from autoconversion (AC), accretion (ACC), melting (MELT), and sinks from evaporation (EVAP), riming (RIM), and rain freezing (FR) with black points indicating the overall budget (i.e., sources minus sinks); (b) percentage contributions of individual process rates to sources and sinks. [Colour figure can be viewed at wileyonlinelibrary.com]

in polluted environments. The by far dominant sink term is the evaporation of raindrops (excluding sedimentation). At both resolutions, the highest total evaporation rates occur in clean environments and are systematically decaying with increasing CCNs concentration. This behaviour can be explained by the fact that when the CCNs concentration is increased the raindrop size distribution shifts to populations that are fewer in number but larger in size. As a result of the smaller surface area of large raindrops relative to their volume, evaporation is reduced (e.g., Storer et al., 2010; Barthlott et al., 2017). Only at 1 km grid spacing does the relative contribution of evaporation decrease with higher aerosol loading, whereas there is no systematic dependence at 2 km grid spacing (Figure 15b). Total riming rates have a negative response to increasing CCNs concentration at 2 km grid spacing but remain rather constant at the finer resolution. Note that this is only rain riming; there is probably a lot of cloud droplet

riming contributing indirectly to the melting terms, and this is strongly decreasing with CCNs; see Barrett and Hoose (2023). The freezing of rain has only small contributions to the budget. The total values, as well as their relative contribution, increase with larger aerosol loading. It is important to note that although less convection is triggered at 2 km grid spacing (see also the results from cloud tracking in Figure 12), the general behaviour of the process rates with respect to different aerosol loads is similar at both model resolutions. Furthermore, the negative effect of aerosols on total precipitation averaged over larger domains that was found in earlier work also holds true for the simulation of individual thunderstorms over complex terrain. This negative aerosol–precipitation effect is not only a consequence of the reduced collision–coalescence process but is also influenced by a reduction in the magnitude of the cold-rain processes. Owing to the greater reduction of warm-rain processes relative to cold-rain processes, the relative importance of the cold-rain processes increases for larger aerosol loadings.

4 | SUMMARY AND CONCLUSIONS

During the Swabian MOSES field campaign, which was conducted in southwestern Germany in summer 2021, a supercell storm formed on June 23, 2021. On this day, a strong southwesterly flow led to a favourable environment for deep convection with sufficient amounts of CAPE and low values of CIN in combination with a strong wind shear. The supercell storm had an exceptionally long lifetime of 7.5 hr, travelled almost 190 km, and impacted large urban and rural areas with strong precipitation and hail. The storm also passed directly over the KITcube main observation site at Rottenburg, where it was observed in detail with remote-sensing radar and lidar and microwave radiometer systems, as well as comprehensive in-situ instruments. The predictability of the event was rather low, as the operational ensemble forecast system showed a large spread and thus provided only a low level of confidence in the future weather development. Hindcasts of this event were performed using two horizontal grid spacings (i.e., 2 km and 1 km) with an operationally used 1MOM and an advanced 2MOM microphysics scheme. The 2MOM scheme allows the study of aerosol effects on mixed-phase clouds and precipitation with CCNs concentrations ranging from low to very high. Numerical results show that all 2 km model realizations do not simulate convective precipitation at the correct location, time, or with the appropriate lifetime. The model run at 1 km grid spacing assuming a low CCNs concentration is able to realistically capture the storm. The location of convection initiation and the simulated cell track towards the northeast show a remarkable agreement

with the observed storm. However, owing to the slower propagation speed in the early stages, the simulated storm has a time delay of 2 hr in the afternoon. At 1 km grid spacing, changes in the aerosol concentration resulted in large changes in convective precipitation, and none of the runs with more polluted environments simulated a supercell storm at the right place or time. By changing the CCNs concentration in a range of $\pm 1\%$, $\pm 2\%$, and $\pm 3\%$ of the clean environment, the robustness of the single successful realization of the event was tested. In all of these runs, a long-lived supercell storm was simulated in the area where the observed supercell occurred, with only minor differences in location and size. The agreement between these runs exploring a larger regime of low CCNs concentrations provides more confidence in the robustness in this result.

Objective forecast verifications measures, such as the fractions skill score with radar-derived precipitation estimates, showed that the 2MOM runs generally perform better than the operational configuration (i.e., 1MOM scheme at 2 km grid spacing). The analysis of domain-averaged convection-related variables showed that a large portion of grid points in the MOSES domain fulfil convection-promoting conditions (i.e., high CAPE in combination with low CIN) with only little sensitivity to grid spacing. Instead, the dependence on the assumed CCNs concentration was found to be much greater: clean environments had the lowest portion of grid points with suitable conditions for deep convection, and an almost systematic increase is simulated in more polluted environments. Low-level wind convergence was much stronger at finer resolution, leading to stronger boundary-layer updraughts that enabled more air parcels to reach their respective LFC to release CAPE.

Observed aerosol particle concentrations indicate that on this day the potential CCNs values were the lowest of the whole month, which suggests that the low aerosol concentration is a reasonable assumption for that case. When comparing the pre-convective thermodynamic environment at Rottenburg, there was a comparatively wide range in the values of CAPE, CIN, and the BRN in the simulations. In all three of these convective indices, the successful model at 1 km grid spacing with low CCNs concentration had the best agreement with radiosonde observations. This indicates that the good model result was obtained for the right reason. Furthermore, the supercell passage at Rottenburg and the surrounding hail sensor network showed comparable features in terms of 2 m temperature drop, hail number concentrations, and maximum hail sizes. The combination of the KITcube rain radars with two DWD radars operating in southwestern Germany enabled a unique composite of four radars in the MOSES domain. The ICON model revealed a large sensitivity of hail to the assumed CCNs concentration, with strongly

decreasing hail amounts for larger aerosol loads. Again, only the 1 km run assuming a low CCNs concentration was able to simulate hail in areas where hail actually occurred. This model run also showed the best agreement with the wind profile observations by Doppler lidar, such as the turning of the inflow and the strong increase in wind speed during the passage of the cell, but not the strong and deep northerly flow after the passage.

The sensitivity of model results to grid resolution was further examined by an automatic tracking of individual storms. In general, there are more convection initiation events at 1 km grid spacing than at the operationally used coarser resolution. The analyses of the distribution of the lifetimes shows that the cells are also longer lived at finer resolution. The negative aerosol effect on the number of convective cells and the large variability in simulated cell tracks are particularly important for flood forecasting, because the precipitation location and intensity are crucial for predicting the amount of precipitation in individual river catchments. The question remains why the 2 km configuration with low CCNs concentration did not reproduce the supercell storm of that day. It turns out that the impact of model grid spacing led to differences in the location and size of earlier convection that impacted the availability of CAPE in the region where the precursors of the supercell formed. The two impacts on CAPE were (a) its consumption due to different convective coverage and intensity and (b) the different strength of warm and moist air transport from the Rhine Valley towards the crest of the southern Black Forest. The initial convection associated with the supercell was then much larger at 1 km grid spacing, and higher CAPE values along with less entrainment of environmental air helped to sustain convection only in this model run.

We computed a rainwater budget analysis and found that melting of frozen hydrometeors is dominating the rain production, followed by accretion with only little contribution from autoconversion. The most important sink term is the evaporation of raindrops, which is largest in clean environments. Higher CCNs concentrations lead to raindrop distributions that are larger in size and therefore less susceptible to evaporation. Although less convection is triggered at 2 km grid spacing, the general behaviour of the process rates with respect to different aerosol loads is similar at both model resolutions. Furthermore, the negative effect of aerosols on total precipitation averaged over larger domains that was found in earlier work also holds true for the simulation of individual thunderstorms over complex terrain. This negative aerosol–precipitation effect is not only a consequence of the reduced collision–coalescence process, but is also influenced by a reduction in the magnitude of the cold-rain processes. Owing to the greater reduction of warm-rain processes relative to cold-rain

processes, the relative importance of the cold-rain processes increases for larger aerosol loads. The negative aerosol–precipitation effect is in contrast to the lower number of grid points with suitable conditions for deep convection (high CAPE and low CIN) found in more polluted environments and indicates that microphysical processes resulting from different CCNs concentrations can have a stronger impact on surface precipitation as aerosol-induced modifications of environmental conditions.

The findings of this study demonstrate the benefits of using an aerosol-aware 2MOM microphysics scheme for convective-scale weather prediction and that CCN assumptions should be carefully chosen if 2MOM schemes are used for modelling aerosol–cloud interactions or quantitative precipitation forecasting. The results presented here are based on a well-observed case from the Swabian MOSES 2021 field campaign but represent only a single case study, which is not sufficient for general conclusions. Although perhaps an extreme example, this case study showed the potential large aerosol impact on cloud evolution and surface precipitation, as the use of different CCNs concentrations can determine whether a supercell is successfully simulated or not.

AUTHOR CONTRIBUTIONS

Christian Barthlott: Conceptualization; data curation; formal analysis; investigation; methodology; software; validation; visualization; writing—original draft; writing—review and editing. **Beata Czajka:** Formal analysis; investigation; writing—original draft. **Michael Kunz:** Formal analysis; investigation; writing—original draft. **Harald Saathoff:** Formal analysis; investigation; writing—original draft. **Hengheng Zhang:** Formal analysis; investigation; writing—original draft. **Alexander Böhmländer:** Formal analysis; investigation; writing—review and editing. **Philipp Gasch:** Formal analysis; investigation; writing—original draft. **Jan Handwerker:** Formal analysis; investigation; writing—review and editing. **Martin Kohler:** Investigation. **Jannik Wilhelm:** Investigation; writing—review and editing. **Andreas Wieser:** Investigation; writing—review and editing. **Corinna Hoose:** Conceptualization; writing—review and editing.

ACKNOWLEDGEMENTS

This work is a contribution to subproject B3 of the Transregional Collaborative Research Center SFB/TRR 165 “Waves to Weather” (<https://www.wavestoweather.de>) funded by the German Research Foundation (DFG) and was supported by funding from the Helmholtz Association within the framework of MOSES. We wish to thank the DWD for providing the ICON model code, the

initial and boundary data, and the RADOLAN and C-band radar data. This work was performed on the HoreKa super-computer with the help of the Large Scale Data Facility at the KIT, both funded by the Ministry of Science, Research and the Arts Baden-Württemberg and by the Federal Ministry of Education and Research. Open Access funding enabled and organized by Projekt

CONFLICT OF INTEREST STATEMENT

On behalf of all the authors, the corresponding author declares that there is no conflict of interest to declare within the article.

DATA AVAILABILITY STATEMENT

The data that support the findings of this study are available from the corresponding author upon reasonable request.

ORCID

Christian Barthlott  <https://orcid.org/0000-0003-2927-5051>

Michael Kunz  <https://orcid.org/0000-0002-0202-9558>

Harald Saathoff  <https://orcid.org/0000-0002-1301-8010>

Jannik Wilhelm  <https://orcid.org/0000-0002-7475-0758>

REFERENCES

- Altaratz, O., Koren, I., Remer, L. & Hirsch, E. (2014) Review: cloud invigoration by aerosols—Coupling between microphysics and dynamics. *Atmospheric Research*, 140–141, 38–60.
- Ashley, W.S., Haberlie, A.M. & Gensini, V.A. (2023) The future of supercells in the United States. *Bulletin of the American Meteorological Society*, 104, E1–E21.
- Barrett, A.I. & Hoose, C. (2023) Microphysical pathways active within thunderstorms and their sensitivity to ccn concentration and wind shear. *Journal of Geophysical Research-Atmospheres*, 128, e2022JD036965.
- Barthlott, C. & Barrett, A.I. (2020) Large impact of tiny model domain shifts for the Pentecost 2014 mesoscale convective system over Germany. *Weather and Climate Dynamics*, 1, 207–224.
- Barthlott, C. & Davolio, S. (2016) Mechanisms initiating heavy precipitation over Italy during the HyMeX special observation period 1: a numerical case study using two mesoscale models. *Quarterly Journal of the Royal Meteorological Society*, 142, 238–258.
- Barthlott, C. & Hoose, C. (2018) Aerosol effects on clouds and precipitation over central Europe in different weather regimes. *Journal of the Atmospheric Sciences*, 75, 4247–4264.
- Barthlott, C., Mühr, B. & Hoose, C. (2017) Sensitivity of the 2014 Pentecost storms over Germany to different model grids and microphysics schemes. *Quarterly Journal of the Royal Meteorological Society*, 143, 1485–1503.
- Barthlott, C., Zarbo, A., Matsunobu, T. & Keil, C. (2022a) Importance of aerosols and shape of the cloud droplet size distribution for convective clouds and precipitation. *Atmospheric Chemistry and Physics*, 22, 2153–2172.
- Barthlott, C., Zarbo, A., Matsunobu, T. & Keil, C. (2022b) Impacts of combined microphysical and land-surface uncertainties on convective clouds and precipitation in different weather regimes. *Atmospheric Chemistry and Physics*, 22, 10841–10860.
- Baur, F., Keil, C. & Barthlott, C. (2022) Combined effects of soil moisture and microphysical perturbations on convective clouds and precipitation for a locally forced case over Central Europe. *Quarterly Journal of the Royal Meteorological Society*, 148, 2132–2146.
- Bechtold, P., Köhler, M., Jung, T., Doblas-Reyes, F., Leutbecher, M., Rodwell, M.J. et al. (2008) Advances in simulating atmospheric variability with the ECMWF model: from synoptic to decadal time-scales. *Quarterly Journal of the Royal Meteorological Society*, 134, 1337–1351.
- Bennett, L.J., Blyth, A.M., Burton, R.R., Gadian, A.M., Weckwerth, T.M., Behrendt, A. et al. (2011) Initiation of convection over the Black Forest mountains during COPS IOP15a. *Quarterly Journal of the Royal Meteorological Society*, 137(S1), 176–189.
- Bouttier, F. & Raynaud, L. (2018) Clustering and selection of boundary conditions for limited area ensemble prediction. *Quarterly Journal of the Royal Meteorological Society*, 144, 2381–2391.
- Bryan, G.H. & Morrison, H. (2012) Sensitivity of a simulated squall line to horizontal resolution and parameterization of microphysics. *Monthly Weather Review*, 140, 202–225.
- Bryan, G.H., Wyngaard, J.C. & Fritsch, J.M. (2003) Resolution requirements for the simulation of deep moist convection. *Monthly Weather Review*, 131, 2394–2416.
- Bunkers, M.J., Johnson, J.S., Czepyha, L.J., Grzywacz, J.M., Klimowski, B.A. & Hjelmfelt, M.R. (2006) An observational examination of Long-lived supercells. Part II: environmental conditions and forecasting. *Weather Forecasting*, 21, 689–714.
- Doms, G., Förstner, J., Heise, E., Herzog, H.-J., Mironov, D., Raschendorfer, M. et al. (2021) A description of the nonhydrostatic regional COSMO-model, Part II: physical parameterizations. <http://www.cosmo-model.org>, 154 pp.
- Done, J., Davis, C. & Weisman, M. (2004) The next generation of NWP: explicit forecasts of convection using the weather research and forecasting (WRF) model. *Atmospheric Science Letters*, 5, 110–117.
- Donner, L.J., O'Brien, T.A., Rieger, D., Vogel, B. & Cooke, W.F. (2016) Are atmospheric updrafts a key to unlocking climate forcing and sensitivity? *Atmospheric Chemistry and Physics*, 16, 12983–12992.
- Fan, J., Leung, L.R., Rosenfeld, D. & DeMott, P.J. (2017) Effects of cloud condensation nuclei and ice nucleating particles on precipitation processes and supercooled liquid in mixed-phase orographic clouds. *Atmospheric Chemistry and Physics*, 17, 1017–1035.
- Fan, J., Wand, Y., Rosenfeld, D. & Liu, X. (2016) Review of aerosol-cloud interactions: mechanisms, significance, and challenges. *Journal of the Atmospheric Sciences*, 73, 4221–4252.
- Groenemeijer, P., Barthlott, C., Behrendt, A., Corsmeier, U., Handwerker, J., Kohler, M. et al. (2009) Observations of kinematics and thermodynamic structure surrounding a convective storm cluster over a low mountain range. *Monthly Weather Review*, 137, 585–602.
- Hande, L.B., Engler, C., Hoose, C. & Tegen, I. (2015) Seasonal variability of Saharan desert dust and ice nucleating particles over Europe. *Atmospheric Chemistry and Physics*, 15, 4389–4397.
- Hande, L.B., Engler, C., Hoose, C. & Tegen, I. (2016) Parameterizing cloud condensation nuclei concentrations during HOPE. *Atmospheric Chemistry and Physics*, 16, 12059–12079.
- Heikenfeld, M., Marinescu, P.J., Christensen, M., Watson-Parris, D., Senf, F., van den Heever, S.C. et al. (2019) Tobac 1.2: towards a

- flexible framework for tracking and analysis of clouds in diverse datasets. *Geoscientific Model Development*, 12, 4551–4570.
- Heise, E., Ritter, B. & Schrodin, E. (2006) Operational implementation of the multilayer soil model TERRA, Technical Report 9. <http://www.cosmo-model.org>, 19 pp
- Hogan, R.J. & Bozzo, A. (2018) A flexible and efficient radiation scheme for the ECMWF model. *Journal of Advances in Modeling Earth Systems*, 10, 1990–2008.
- Kalthoff, N., Adler, B., Wieser, A., Kohler, M., Träumner, K., Handwerker, J. et al. (2013) KITcube—a mobile observation system for convection studies deployed during HyMeX. *Meteorologische Zeitschrift*, 22, 633–647.
- Kärcher, B., Hendricks, J. & Lohmann, U. (2006) Physically based parameterization of cirrus cloud formation for use in global atmospheric models. *Journal of Geophysical Research*, 111, D01205.
- Kärcher, B. & Lohmann, U. (2002) A parameterization of cirrus cloud formation: homogeneous freezing of supercooled aerosols. *Journal of Geophysical Research*, 107, AAC 4–1–AAC 4–10.
- Keil, C., Baur, F., Bachmann, K., Rasp, S., Schneider, L. & Barthlott, C. (2019) Relative contribution of soil moisture, boundary-layer and microphysical perturbations on convective predictability in different weather regimes. *Quarterly Journal of the Royal Meteorological Society*, 145, 3102–3115.
- Kohler, M., Kalthoff, N. & Kottmeier, C. (2010) The impact of soil moisture modifications on CBL characteristics in West Africa: a case-study from the AMMA campaign. *Quarterly Journal of the Royal Meteorological Society*, 136, 442–455.
- Kulmala, M., Kokkonen, T., Ezhova, E., Baklanov, A., Mahura, A., Mammarella, I. et al. (2023) Aerosols, clusters, greenhouse gases, trace gases and boundary-layer dynamics: on feedbacks and interactions. *Boundary-Layer Meteorology*, 186, 475–503.
- Kunz, M., Abbas, S.S., Bauckholt, M., Böhmländer, A., Feuerle, T., Gasch, P. et al. (2022) Swabian MOSES 2021: an interdisciplinary field campaign for investigating convective storms and their event chains. *Frontiers in Earth Science*, 10, 999593.
- Kunz, M. & Puskeiler, M. (2010) High-resolution assessment of the hail hazard over complex terrain from radar and insurance data. *Meteorologische Zeitschrift*, 19, 427–439.
- Leuenberger, D., Koller, M., Fuhrer, O. & Schär, C. (2010) A generalization of the SLEVE vertical coordinate. *Monthly Weather Review*, 138, 3683–3689.
- Markowski, P. & Richardson, Y. (2011) *Mesoscale meteorology in Mid-latitudes*. Advancing Weather and Climate Science. Chichester, UK: John Wiley & Sons Ltd. <https://books.google.de/books?id=MDeYosfLLEYC>
- Matsunobu, T., Keil, C. & Barthlott, C. (2022) The impact of microphysical uncertainty conditional on initial and boundary condition uncertainty under varying synoptic control. *Weather and Climate Dynamics*, 3, 1273–1289.
- May, R.M., Arms, S.C., Marsh, P., Bruning, E., Leeman, J.R., Goebert, K. et al. (2022) Metpy: a python package for meteorological data. <https://github.com/Unidata/MetPy>
- Meißner, C., Kalthoff, N., Kunz, M. & Adrian, G. (2007) Initiation of shallow convection in the Black Forest mountains. *Atmospheric Research*, 86, 42–60.
- Noppel, H., Blahak, U., Seifert, A. & Beheng, K.D. (2010) Simulations of a hailstorm and the impact of CCN using an advanced two-moment cloud microphysical scheme. *Atmospheric Research*, 96, 286–301.
- Puskeiler, M., Kunz, M. & Schmidberger, M. (2016) Hail statistics for Germany derived from single-polarization radar data. *Atmospheric Research*, 178–179, 459–470.
- Raschendorfer, M. (2001) The new turbulence parameterization of LM, COSMO Newsletter 1, 89–97. <http://www.cosmo-model.org>, 115 pp
- Richard, E., Chaboureaud, J.P., Flamant, C., Champollion, C., Hagen, M., Schmidt, K. et al. (2011) Forecasting summer convection over the Black Forest: a case study from the convective and Orographically-induced precipitation study (COPS) experiment. *Quarterly Journal of the Royal Meteorological Society*, 137(S1), 101–117.
- Roberts, N.M. & Lean, H.W. (2008) Scale-selective verification of rainfall accumulations from high-resolution forecasts of convective events. *Monthly Weather Review*, 136, 78–97.
- Rosenfeld, D., Lohmann, U., Raga, G., O'Dowd, C., Kulmala, M., Fuzzi, S. et al. (2008) Flood or drought: how do aerosols affect precipitation? *Science*, 321, 1309–1313.
- Schneider, L., Barthlott, C., Barrett, A.I. & Hoose, C. (2018) The precipitation response to variable terrain forcing over low-mountain ranges in different weather regimes. *Quarterly Journal of the Royal Meteorological Society*, 144, 970–989.
- Schneider, L., Barthlott, C., Hoose, C. & Barrett, A.I. (2019) Relative impact of aerosol, soil moisture, and orography perturbations on deep convection. *Atmospheric Chemistry and Physics*, 19, 12343–12359.
- Schwartz, C.S., Romine, G.S., Fossell, K.R., Sobash, R.A. & Weisman, M.L. (2017) Toward 1-km ensemble forecasts over large domains. *Monthly Weather Review*, 145, 2943–2969.
- Segal, Y. & Khain, A. (2006) Dependence of droplet concentration on aerosol conditions in different cloud types: application to droplet concentration parameterization of aerosol conditions. *Journal of Geophysical Research*, 111, D15240.
- Seifert, A. & Beheng, K.D. (2006) A two-moment cloud microphysics parameterization for mixed-phase clouds. Part I: model description. *Meteorology and Atmospheric Physics*, 92, 67–82.
- Storer, R.L., van den Heever, S.C. & Stephens, G.L. (2010) Modeling aerosol impacts on convective storms in different environments. *Journal of the Atmospheric Sciences*, 67, 3904–3915.
- Tao, W.-K., Chen, J.-P., Li, Z., Wang, C. & Zhang, C. (2012) Impact of aerosols on convective clouds and precipitation. *Reviews of Geophysics*, 50, RG2001.
- Thompson, G., Berner, J., Frediani, M., Otkin, J.A. & Griffin, S.M. (2021) A stochastic parameter perturbation method to represent uncertainty in a microphysics scheme. *Monthly Weather Review*, 149, 1481–1497.
- Tiedtke, M. (1989) A comprehensive mass flux scheme for cumulus parameterization in large-scale models. *Monthly Weather Review*, 117, 1779–1800.
- van den Heever, S.C., Stephens, G.L. & Wood, N.B. (2011) Aerosol indirect effects on tropical convection characteristics under conditions of radiative-convective equilibrium. *Journal of the Atmospheric Sciences*, 68, 699–718.
- Warren, R., Kirshbaum, D., Plant, R. & Lean, H. (2014) A 'Boscastle-type' quasi-stationary convective system over the UK southwest peninsula. *Quarterly Journal of the Royal Meteorological Society*, 140, 240–257.
- Weber, U., Attinger, S., Baschek, B., Boike, J., Borchardt, D., Brix, H. et al. (2022) MOSES: a novel observation system to monitor

- dynamic events across earth compartments. *Bulletin of the American Meteorological Society*, 103, E339–E348.
- Weisman, M.L., Davis, C., Wang, W., Manning, K.W. & Klemp, J.B. (2008) Experiences with 0–36-h explicit convective forecasts with the WRF-ARW model. *Weather Forecasting*, 23, 407–437.
- Weisman, M.L. & Klemp, J.B. (1982) The dependence of numerically simulated convective storms on vertical wind shear and buoyancy. *Monthly Weather Review*, 110, 504–520.
- Weisman, M.L., Manning, K.W., Sobash, R.A. & Schwartz, C.S. (2023) Simulations of severe convective systems using 1- versus 3-km grid spacing. *Weather Forecasting*, 38, 401–423.
- Wulfmeyer, V., Behrendt, A., Kottmeier, C., Corsmeier, U., Barthlott, C., Craig, G.C. et al. (2011) The convective and Orographically induced precipitation study (COPS): the scientific strategy, the field phase, and first highlights. *Quarterly Journal of the Royal Meteorological Society*, 137(S1), 3–30.
- Zängl, G., Reinert, D., Ripodas, P. & Baldauf, M. (2015) The ICON (ICOsahedral non-hydrostatic) modelling framework of

DWD and MPI-M: description of the non-hydrostatic dynamical core. *Quarterly Journal of the Royal Meteorological Society*, 141, 563–579.

How to cite this article: Barthlott, C., Czajka, B., Kunz, M., Saathoff, H., Zhang, H., Böhmländer, A. et al. (2024) The impact of aerosols and model grid spacing on a supercell storm from Swabian MOSES 2021. *Quarterly Journal of the Royal Meteorological Society*, 1–23. Available from: <https://doi.org/10.1002/qj.4687>